A STUDY OF THE $Li^7(He^3,n)B^9$ REACTION BY TIME-OF-FLIGHT TECHNIQUES

Thesis by

Frank Sigel Dietrich, III

In Partial Fulfillment of the Requirements

for the Degree of

Doctor of Philosophy

California Institute of Technology

Pasadena, California

1964

(Submitted May 19, 1964)

ACKNOWLEDGMENTS

The author gratefully acknowledges the encouragement and advice of the staff of the Kellogg Radiation Laboratory, especially that of Professors C. A. Barnes, R. W. Kavanagh, and T. Lauritsen. It is a particular pleasure to acknowledge the instruction and advice of Dr. Lawrence Cranberg, who introduced the author to the techniques of neutron time-of-flight spectroscopy at the Los Alamos Scientific Laboratory during the summers of 1959-60. The author wishes to thank Mr. J. W. Davies for assistance with the apparatus, and Mr. J. L. Honsaker for participation in the early stages of the experiment. The author also wishes to express his gratitude to the National Science Foundation for a series of fellowships which supported him during most of the work, and to the joint program of the Office of Naval Research and the United States Atomic Energy Commission, which supported the research.

ABSTRACT

The $Li^7(He^3, n)B^9$ reaction has been investigated at incident energies from 5.2 to 12.5 Mev, using a pulsed-beam time-of-flight spectrometer in conjunction with the ONR-CIT tandem accelerator. The spectrometer includes a pre-acceleration beam-bunching system, which increases the average target current by a factor of approximately 10 for protons and deuterons, and 4 for He^3 and alpha beams. Previously unreported B^9 levels were found at the energies listed below, together with their widths:

E_x (Mev)	Γ (kev)
12.06 ± 0.06	800 ± 200
14.01 ± 0.07	390 ± 110
14.668 ± 0.016	< 45
16.022 ± 0.025	180 ± 16

At 12.5-Mev bombarding energy, neutron groups corresponding to known B^9 states at 17.19 and 17.63 Mev were observed. No other B^9 states were resolved below 17.9-Mev excitation. The neutron groups were superimposed on an intense background continuum, attributable to processes leading to the final configuration $2\alpha + p + n$. An angular distribution at 8.7-Mev incident energy of neutrons leading to the 14.67-Mev state is roughly isotropic in the

center-of-mass system, and the total cross section is 8 mb. A $T = 3/2$ assignment for the 14.67-Mev state is suggested by its narrow width, and by recent studies of the $Li^7(t,p)Li^9$ and $Li^7(He^3,p)Be^9$ reactions. A comparison of the $Li^7(He^3,p)Be^9$ and $Li^7(He^3,n)B^9$ reactions shows that the cross sections for formation of the 14.67-Mev B^9 state and the analogous Be^9 state are approximately equal, if barrier-penetration effects in the outgoing channels are removed.

TABLE OF CONTENTS

I. INTRODUCTION

Experimental data for the mass-nine nuclei are conspicuously meager. Part of the difficulty lies in the energetics of the available reactions, and part is due to prolific backgrounds produced by the multiparticle breakup channels that accompany nearly all the reactions.

Figure 1 shows the presently known levels of B^9. Prior to the work reported herein, the structure of B^9 had been studied extensively only in the regions of excitation below about 5 Mev and above 17 Mev. It is difficult to explore highly excited states with reactions producing B^9 as a residual nucleus, since the negative Q-values of most of these reactions require bombarding energies beyond the capabilities of presently available electrostatic accelerators. Reactions in which B^9 serves as the compound nucleus can be used to study B^9 structure only above the Be^7 + d threshold near 16.5 Mev. Two reactions with sufficiently high ground-state Q-value to bridge the 5- to 17-Mev gap are $Li^7(He^3, n)B^9$ (Q = 9.347 Mev) and $B^{10}(He^3, \alpha)B^9$ (Q = 12.137 Mev). Previous studies of both reactions at low bombarding energies have shown clear structure only for excitation energies below 4 Mev, even though B^9 levels up to 12 or 15 Mev could have been excited (Ajzenberg-Selove and Lauritsen, 1965). The ONR-CIT tandem accelerator with helium ion injector

produces incident He^3 energies up to about 12.5 Mev, which is enough to excite B^9 states up to more than 18 Mev with both reactions.

The stimulus for the present work came from an investigation of the $Li^7(He^3,p)Be^9$ reaction by Lynch, Griffiths, and Lauritsen (1964), which established a level in Be^9 at 14.39 Mev excitation with width less than 5 kev. The narrow width of the state and recent information about the mass of Li^9 (Middleton and Pullen, 1964) suggested that the state was probably the first T = 3/2 level in Be^9. The present study of the $Li^7(He^3,n)B^9$ reaction was undertaken to search for the mirror analogue of the 14.39-Mev Be^9 state and to investigate any other structure at high excitation energies in B^9. In addition to the expected narrow state at 14.67 Mev, three previously unreported levels were seen at 12.06, 14.0, and 16.02 Mev excitation. These results led Fisher and Whaling (1963) to investigate the same region of B^9 excitation with the $B^{10}(He^3,\alpha)B^9$ reaction. Their spectra show only the ground and 2.34-Mev states, and a new state at 11.62 Mev.

Figure 2 summarizes the results of recent experimental investigations of the mass-nine level schemes. The square-bracketed numbers give the energies of the ground states of Li^9 and B^9 relative to the ground state of Be^9, after correction has been

made for Coulomb energy and the neutron-proton mass difference according to the formula

$$1.2\ \frac{Z-1}{A^{1/3}}\ -\ 0.78\ \text{Mev}\ ,$$

where Z is the higher atomic number of each pair Li^9-Be^9 and Be^9-B^9 (Ajzenberg-Selove and Lauritsen, 1963).

Neutron spectra from the $Li^7(He^3,n)B^9$ reaction are complicated by intense yields of continuum neutrons from competing reactions and from multibody breakups of the B^{10} intermediate system. Figure 3 shows the mass excesses of all combinations of particles that can be formed by He^3 bombardment of Li^7 at energies up to 15 Mev. For simplicity, only ground state energies of the nuclear clusters are shown. All reactions in which a neutron is produced must lead to the configuration $2\alpha + p + n$. Since the $Li^7(He^3,n)B^9$ reaction is only one of many processes leading to $2\alpha + p + n$, it must compete with sequential reactions such as $Li^7 + He^3 \rightarrow Be^9(E_x = 2.43\ \text{Mev}) + p \rightarrow Be^8 + p + n$, and multiparticle breakups such as $Li^7 + He^3 \rightarrow Be^8 + p + n$. Neutron groups corresponding to states in B^9 can be separated from competing processes only by kinematics, and care must be taken to ensure that no neutron groups can be produced in alternative reactions which are sufficiently sharp to be confused with B^9 structure.

The neutron spectra from the $Li^7 + He^3$ reactions were studied by using a pulsed-beam time-of-flight spectrometer in conjunction with the ONR-CIT tandem accelerator. The resolution of a time-of-flight spectrometer is best for low neutron energies, and deteriorates rapidly with increasing energy. The available resolution was sufficient to resolve B^9 structure at excitation energies in the 10 to 17 Mev region, but not adequate to separate the ground state or any other low-lying structure from the continuum neutrons. An unusual feature of the time-of-flight system is the use of pre-acceleration beam bunching to increase the average target current. The buncher is described in detail in Part II and in Appendix B.

II. EXPERIMENTAL TECHNIQUES AND APPARATUS

1. Introduction

Measurement of neutron energies by time of flight requires a time comparison of two signals, one characteristic of the time that a neutron strikes the detector, and the other characteristic of the time that it was produced at the target. The detector signal can be obtained in a straightforward fashion from proton recoils in a fast organic scintillator viewed by a fast photomultiplier. The most versatile means of obtaining the target signal is the pulsed-beam method, as described in the review articles by Cranberg and Rosen (1960), and Neiler and Good (1960).

Figure 4 shows schematically the principal components of the time-of-flight system installed in the ONR-CIT tandem. The components may be divided into three groups: beam-handling units, an r. f. system, and a data-collecting system, which includes the neutron detector, time-to-pulse-height converter, and data storage equipment.

2. Beam-Handling Components

The beam burst duration is fixed by deflecting the high energy particle beam across a set of beam-catching slits positioned close to the 90° analyzer object slits. The beam is swept

vertically, in order to avoid deflecting it across the accelerator regulating slits. The deflector plates are 58 inches long, 2 inches wide, and are separated by 13/16 inch. The distance between the beam-catching slits and the near end of the deflecting plates is approximately 28 inches. The 3.531-Mc sinusoidal r. f. voltage applied to the plates is capable of chopping any available beam to less than 2 ns with a beam-catching slit separation of 0.2 inch.

It has been observed that the chopped beam is always split vertically into two components, each of which corresponds to passage of the beam across the slits in one of the two directions. The splitting is related to the transit time of the particles through the deflector plates. If the beam is correctly aligned with deflection voltage off, the beam passes midway between the deflection plates and through the beam-catching slits. When deflection voltage is turned on, each beam burst must enter the deflection plates midway between them and must pass through the chopping slits; but since the r. f. deflection voltage is zero only instantaneously, each burst must traverse a curved path through the system, and receive an angular deflection at exit. Symmetry requires that the angular deflections must be equal and opposite for bursts corresponding to the positive- and negative-going zeros of the r. f. waveform. The trajectories are illustrated in Figure 5a. By careful adjustment of the accelerator deflection controls, one of the chopped beam

components can usually be prevented from reaching the target altogether. This is a desirable feature, since the buncher produces only one bunched pulse per r. f. cycle.

There are separate bunchers for the helium and hydrogen isotopes, although for simplicity only one is shown in Figure 4. The proton-deuteron buncher is located between the negative-ion source and the tandem tank, at a distance of about 12 feet from the entrance to the accelerating column. The He^3-alpha buncher is positioned between the small electrostatic accelerator, which supplies positive helium ions, and the negative-ion source box, where the ions are neutralized. The distance from the helium buncher to the stripping canal at the tandem's high-energy terminal is about 38 feet. The proton-deuteron buncher obviously cannot serve for helium isotopes, because the helium beams are neutral when they pass through it.

The bunching scheme employed, which is similar to that developed independently by Lefevre, Borchers, and Poppe (1962), is shown schematically in Figure 5b. The beam travels along the common axis of the two adjacent brass cylinders separated by a narrow gap. If a sinusoidal voltage $V_o \sin \omega t$ is applied to the cylinders as shown, and if the length of each cylinder is chosen so that the phase of the voltage advances by a half cycle while the ions drift through it, then the beam energy will be modulated by

$4q V_o \sin \omega t$ on either side of the initial energy, where q is the ionic charge. The corresponding velocity modulation causes bunching of the beam at the target. The bunching must take place almost entirely within the distance from the buncher to the point at which acceleration begins, since the flight time to the target decreases rapidly as the beam gains energy.

The buncher tubes are constructed of brass cylinders of 1.5 — inches inside diameter to ensure beam clearance. The cylinder length required for the bunching of 400-kev alpha particles is 24 inches. Additional short lengths may be electrically attached to the outside ends of the alpha-bunching cylinders to increase their length to the 28 inches required for bunching He^3 ions of the same energy. The buncher for the 53-kev proton and deuteron beams is of similar construction.

The optimum r. f. voltages are about 1 kv and 5 kv peak for the p-d and α-He^3 bunchers, respectively. Although the total energy spread introduced into the beam is 8 times the peak voltage, the energy spread in the target beam pulse is much smaller, because heavily velocity-modulated particles fall in the portion of the beam cycle which is thrown away by the high-energy deflectors. The energy spread at target is about 1.6 kev for protons and deuterons, and 10 kev for He^3 and alpha particles.

The increase in average target current gained by using the

bunchers is typically a factor of 10 for protons and deuterons, and 4 for He^3. These factors are for pulse durations of about 3 ns and 5 ns, respectively.

Details of buncher design and performance are discussed in Appendix B.

3. The R. F. System

The r. f. system provides properly phased r. f. power for the bunchers and the high-energy deflectors, and supplies a suitably shaped stop pulse to the time-to-pulse-height converter.

The r. f. frequency is determined by a 3.531-Mc crystal-controlled oscillator, which has several independent cathode-follower outputs. One of the outputs is fed directly to the r. f. amplifiers for the high-energy deflector plates, and another is fed to the buncher r. f. amplifiers through a variable phase-shift device containing a commercially-built potentiometer-type delay line.

The buncher and deflector r. f. amplifiers have very similar push-pull power output stages, of approximately 350 and 1500 watts plate power input, respectively. The output circuits are r. f. transformers having untuned primaries and tuned secondaries, as shown in Figure 5b for the buncher.

The time-to-pulse-height converter stop pulse must be

synchronized accurately with the target beam pulse, since any jitter in the time difference between these two events will impair the resolution of the system. A jitter-free timing signal is picked up by a one-turn loop inductively coupled to the secondary of the r. f. transformer in the deflector output circuit. This signal is routed through a variable phase-shifter, amplified, squared, clipped by a shorted delay line, and amplified again by a HP460B wide-band amplifier. The resulting shaped stop pulse has an amplitude of -15 to -20 volts and a width of about 30 ns.

It is often more convenient to derive the timing signal directly from one of the oscillator outputs, since then the detector and counting electronics may be tested without turning on the deflector voltage. Although this method has proved satisfactory for most experiments, a slight broadening of the time resolution can be noticed for beam pulse widths of duration comparable with the time resolution of the detector electronic circuitry (about 2 ns).

4. The Data-Collecting System

The neutrons are detected by proton recoils in a 5-inch diameter by 2-inch thick Pilot B plastic scintillator viewed by a 5-inch diameter 58AVP phototube. The gamma background is reduced by placing the phototube inside a cylindrical lead shield of 1 5/8-inch thickness. A 1/4-inch thick lead disk positioned in front

of the scintillator attenuates low-energy gammas entering the face of the detector. The disk removes only about one-tenth of the neutrons incident on the detector face. The detector and lead shielding are housed in a large (6-1/2 inch thick) neutron collimator consisting of a uniform mixture of lithium carbonate and paraffin. Neutrons entering the sides of the collimator are attenuated by a factor of 7 to 10.

The fast timing signal ("start pulse") is derived from the 58AVP anode pulse. The anode pulse is clipped by an 8-foot, 125-ohm shorted coaxial cable, then limited and inverted. Since the down-and-back time of the clipping line is about half the width of the anode pulse, the clipped pulse crosses through zero after the initial negative swing. It has been shown in practice (Lefevre and Russell, 1958) that the zero-crossing pulse provides a start pulse whose timing is much less sensitive to anode pulse height than the unclipped pulse. The start pulses caused by energetic proton recoils are negative, of amplitude greater than 2.5 volts, and have a rise time less than 3 ns. The pulse duration is in the range 30 to 60 ns.

The time-to-pulse-height converter is a commercially available version (Eldorado Model 300) of the Los Alamos circuit (Weber, Johnstone, and Cranberg, 1956). The converter output pulses are proportional to the interval between the arrival of a detector pulse at the "start" input and the following stop pulse.

The output spectrum is stored in a RIDL 400-channel pulse height analyzer. The scale (time per channel) of the presentation is adjusted by varying the gain of the converter output-pulse inverting amplifier.

Phototube noise, low-energy gamma rays, and proton-recoil pulses of small amplitude are biased out by a side-channel discriminator system. A "linear" signal taken from the 12th phototube dynode is fed to a double-delay-line-clipped amplifier and discriminator (Hamner N328). The discriminator output pulses gate the multichannel analyzer at its delayed coincidence input.

5. Performance of the Apparatus

The time resolution of the system is limited by the detector time resolution and the beam burst duration. The detector time resolution is shortest for gamma rays (about 1.8 ns), and somewhat longer for low-energy neutrons. The best resolution observed for 1-Mev neutrons was about 2.5 ns.

The steady-state currents for protons and deuterons were 0.7 to 3 μa. The average beam current resulting from bunching a 1 μa continuous beam and chopping it to a pulse duration of about 3 ns was typically 0.1 μa. The overall time resolution was then slightly greater than 3 ns. The steady-state current for He^3 was 0.5 to 1 μa. Because of the low bunching factor, it was necessary

to increase the burst duration to 4 or 5 ns in order to obtain usable currents. Typical average He^3 currents were in the range 0.015 to 0.050 μa, with an overall time resolution of 5 ns.

6. General Features of Time-of-Flight Spectra

All time-of-flight spectra are stored in 100-channel quadrants of the 400-channel analyzer. The numbering of the 100 channels of each quadrant will be taken as 0 to 99. Flight time begins at a channel χ_o and increases linearly toward smaller channels. The time per channel τ_c is set by the multi-channel analyzer controls and by the inverting amplifier. τ_c remains constant at about 1.86 ns/channel throughout all the work described in this thesis. On the other hand, the zero-time channel χ_o depends on the stop-pulse phasing and may vary from run to run. χ_o is ordinarily set near the right-hand edge of the spectrum.

In the simple spectrum of Figure 9, χ_o is at channel 88.5. The gamma peak appears a few channels to the left of χ_o, at channel 85.2. The gamma peak is usually very prominent, since all gammas produced by the beam burst at target have the same flight time. The peak at channel 34.1 is caused by 1.75-Mev neutrons from the $Li^7(p,n)Be^7$ (ground state) reaction, and the peak at channel 25.5 is due to 1.285-Mev neutrons corresponding to the first excited state of Be^7 at 0.432 Mev. The example also shows

the tendency of sharp groups to tail off less sharply on the left-hand side than on the right.

Figure 10 illustrates features of a more complicated spectrum. During a long run, an appreciable time-independent background may accrue from tube noise pulses, background radiation, and neutrons that have traversed complex paths. The size of this background may be estimated by examining the region of the spectrum near the gamma peak. A spurious gamma peak (channel 14.5 in the example) is occasionally observed about 72 channels to the left of the true gamma peak. This peak results from insufficient suppression of the beam burst occurring when the high energy deflectors sweep the beam across the chopping-slit aperture during the "debunched" part of the r. f. cycle. Discrete neutron groups corresponding to B^9 levels are visible above a continuum.

The portion of all spectra below channel 12 is unreliable, and should be ignored.

The details of extracting information from time-of-flight spectra, including consideration of time-scale nonlinearities, are discussed in Appendix A.

7. Detector Efficiency and Calibration

The neutron detector efficiency is determined by the composition and geometry of the scintillation crystal, and by the bias

setting of the side-channel discriminator. Figure 11 shows a Cs^{137} gamma-ray spectrum taken from the linear output of the detector, with the 1/4-inch lead disk removed from the face of the crystal. The side-channel discriminator threshold is set so as to reject pulses of amplitude smaller than those half-way down the right-hand edge of the gamma peak (about channel 110). The gain of the amplifier preceding the discriminator unit is then multiplied by eight before taking neutron spectra. The resultant threshold for proton recoils is approximately 450 kev.

The relative detector efficiency was measured by observing the neutron yield from the $Li^7(p,n)Be^7$ and $T(p,n)He^3$ reactions. Relative differential cross sections for both of these reactions are known (Bevington et al., 1961; Gabbard et al., 1959). The points in Figure 12 show the relative sensitivity for low-energy neutrons measured with the $Li^7(p,n)Be^7$ (ground state) reaction. The $T(p,n)He^3$ reaction was used to measure the relative sensitivity for neutrons from 1.5 to 5.5 Mev. A standard Oak Ridge National Laboratory tritium-zirconium target mounted so that it could be cooled directly from the back was used. The target appeared to be uniform to about 15% over its central region, and no tritium loss was observed with average target currents of 0.1 μa and incident energies up to 6.5 Mev. The results showed that the relative sensitivity is maximum around 1.7 Mev, and is constant to within

$\pm$ 10% in the 1- to 3-Mev region. The relative sensitivity at higher energies decreases slowly with the decrease in the n-p scattering cross section.

If it is assumed that the crystal is thin and that scattering from carbon may be neglected, an approximation to the detector efficiency is

$$\epsilon(E_n) = \frac{E_n - E_o}{E_n} \left\{1 - e^{-nt\sigma(E_n)}\right\}, \qquad (1)$$

where E_n is the incident neutron energy, E_o is the side-channel discriminator threshold energy, n is the number of hydrogen atoms per unit volume, t is the crystal thickness, and σ is the neutron-proton scattering cross section. For computational purposes, $\sigma(E_n)$ may be approximated by the expression (Kavanagh, 1963)

$$\sigma(E_n) = 4.8\, E_n^{-\frac{1}{2}} - 0.55 \text{ barns}, \qquad (2)$$

where E_n is in Mev. Remarkably enough, the measured detector sensitivity curve is fitted to about $\pm$ 10% up to E_n = 5.5 Mev by choosing E_o = 0.45 Mev and nt = 0.2645 barns^{-1}. The fit is shown by the solid curve in Figure 12.

An accurate determination of absolute detector efficiency was not required, since errors in the absolute sensitivity enter into the

experimental results only through small corrections to the measured Q-values due to target thicknesses. The absolute sensitivity of a detector with almost identical geometry, composition, and bias setting was measured at Los Alamos, and its maximum efficiency was found to be 0.35 ± 0.03 for 1.8 Mev neutrons (Zafiratos, 1963). The efficiency of the detector used at Caltech should be very nearly the same. Expression (1) predicts an efficiency of 0.4 for 1.8 Mev neutrons.

In an early part of the work, the system was set up with a bias $E_o = 0.65$ Mev. The spectra of Figures 19-22 were taken with $E_o = 0.65$ Mev; for all other spectra presented in this thesis, $E_o = 0.45$ Mev.

8. Lithium Target Preparation and Charge Collection

The lithium targets used in the experiments were 99.994%-pure Li^7 metal, evaporated in situ on a 0.02-inch tantalum backing. The chunks of lithium metal were cleaned under kerosene, rapidly transferred to the evaporation boat, and pumped at a pressure of 10^{-5} to 10^{-6} torr for several hours before evaporation. Targets of roughly 20- to 100-kev thickness for 8.7-Mev He^3 could be evaporated easily. No progressive loss of lithium was observed with currents of less than 1 μa at 8.7-Mev bombarding energy. Local variations in target thickness, as measured by successive runs of the $Li^7(p,n)Be^7$ reaction, appeared to be about 10%.

The target was held at a potential of 300 volts above ground, and a loop of wire on the outside of the portion of the glass "T" assembly just ahead of the target was kept at -300 volts. No changes in measured beam current were noticed until both voltages were reduced below 100 volts. The charge was collected by an Eldorado Model CI-110 current integrator.

III. PRESENTATION OF DATA

1. Introduction

Li^7 targets were bombarded with He^3 beams of 5.2 to 12.5 Mev. Although it was possible to excite B^9 levels up to 18.10 Mev at the highest bombarding energies, the low-energy cutoff of the neutron detector limits the maximum excitation energy at which neutron groups may be seen in the spectra. If the neutrons are required to have an energy of 1 Mev or greater, the maximum observable excitation energy is about 17.9 Mev at 0° observation angle and 12.5-Mev incident energy.

The levels at 12.06, 14.0, 14.67, and 16.02 Mev excitation were found in spectra at incident energies of 11.0 Mev and lower. A single spectrum taken at 12.5 Mev and 0° shows weak neutron groups corresponding to known levels at 17.19 and 17.63 Mev, but no other B^9 structure other than that seen at the lower energies. The lowest bombarding energy at which useful results were obtained was 6.25 Mev. The 12.06-Mev level can be seen in the 5.2-Mev spectra, but the neutron energies in the low-energy tail of the peak fall in the rapidly changing portion of the relative sensitivity curve.

The errors quoted in this part may be interpreted as standard deviations.

2. Identification of States

Neutron spectra taken at 0° and 40° with incident energy 8.7 Mev are shown in Figures 13 through 16. Figures 14 and 16 are portions of Figures 13 and 15 converted to a counts-vs.-energy presentation by the computer program described in Appendix A. These spectra show the states observed at 12.06, 14.0, and 14.67 Mev. The channel locations and energies of the neutron groups corresponding to the levels are listed in Table I and in the figure captions. The 14.0-Mev level is easily distinguished only in the counts-vs.-energy spectra, but may be seen as an inflection in the steeply rising continuum in the time spectra. Figures 17 and 18 are spectra taken with an incident energy of 11.0 Mev at 0° and 30°. In addition to the 12.06-and 14.67-Mev peaks, the spectra show groups corresponding to the 16.02-Mev level.

Identification of the groups as corresponding to states of B^9 is made by observing the change in energy of the groups with angle of observation. The last two columns of Table I exhibit the results of calculating the residual nucleus mass from the peak positions in Figures 13-18. The last column shows the change in calculated residual mass that results from a one-channel change in the assumed

peak position at the larger angle. The mass-nine identification is very good for the 14.67-and 16.02-Mev levels. The mass identification of the 14.0-Mev level is somewhat obscured by the considerable breadth of the neutron group. Nevertheless, if we assume a two-channel error in locating the centers of the peaks, it is only necessary to eliminate the possibility of target contaminants of mass 6 to 10 to make identification certain. It is concluded in Section 8 below that there is no evidence for contaminants in this mass region.

The residual mass for the 12.06-Mev level is poorly defined by the 8.7-Mev runs, not only because of the width of the group, but also because the resolution is inferior at high neutron energies. Spectra taken at incident energies of 7.14 and 6.25 Mev determine the residual mass accurately. The 7.14-Mev spectra are shown in Figures 19-22. At 0°, the peak occurs at $\chi_n = 28$ with $E_n = 3.30$ Mev. At 45°, $\chi_n = 26$ and $E_n = 2.70$ Mev. The calculated residual mass is $M_{res} = 9.1$, and $\Delta M_{res}/\Delta\chi_n = 1.5$.

The only other well-defined feature of the neutron spectra is the right-hand endpoint of the continuum. The endpoint energy is always consistent with the formation of B^9 in the ground state ($Q = 9.347$ Mev), and for the breakup reaction $Li^7 + He^3 \rightarrow 2\alpha + p + n$ ($Q = 9.628$ Mev). The peak which often occurs on the plateau between the 12.06-Mev peak and the continuum endpoint may be structure in B^9 in the 7- to 10-Mev region. In Figure 21, for

example, the peak at $\chi_n = 54$ corresponds to $E_x = 7.5$ Mev in B^9. In Figure 13, the peak at $\chi_n = 70$ corresponds to $E_x = 9.1$ Mev, while the sharp corner on the continuum at $\chi_n = 73$ would have $E_x = 7.1$ Mev.

3. The 14.67-Mev Level

The best Q-value and an upper limit for the width of the 14.67-Mev level are found from the spectra of Figures 23-25. The 2.7-Mev incident energy for the $Li^7(p,n)Be^7$ spectrum (Figure 25) was chosen so that the energy of the Be^7 ground-state neutron group would lie very close to the energy of the group from the 14.67-Mev state in the B^9 spectrum. The two spectra were taken within an hour of each other, and with identical target and geometry. An accurate value for the Q of the B^9 state is obtained by comparing directly the neutron and gamma peak positions of the two spectra. In this manner, errors resulting from time-to-pulse-height-converter nonlinearity, flight-path and angle measurements, and long-term electronic drifts are eliminated.

We assume incident energies of 8.006 Mev for the He^3 beam, and 2.702 Mev for the proton beam. The channel assignments are $\chi_n = 19.5$ and $\chi_\gamma = 97.0$ for the B^9 spectrum, and $\chi_n = 18.5$ and $\chi_\gamma = 93.9$ for the Be^7 spectrum. The preliminary Q-value for the B^9 state is -5.340 ± 0.009 Mev, where the error

represents a one-half-channel uncertainty in determining the differences $(\chi_\gamma - \chi_n)$ for each spectrum.

Target thickness is estimated by observing the yield of the $Li^7(p,n)Be^7$ ground-state peak, correcting it for detector efficiency, and comparing it with the known cross section. The detector efficiency for 1-Mev neutrons is assumed to be 0.32 ± 0.08 (see Section 6, Part II). Taking the 0° differential cross section for the $Li^7(p,n)Be^7$ reaction to be 57 mb/sr at $E_p = 2.7$ Mev (Bevington, Rolland, and Lewis, 1961), and the number of counts in the Be^7 neutron peak to be 6.11×10^4, the target density is $(1.15 \pm 0.3) \times 10^{19}$ lithium atoms/cm^2. McCray (1962) has demonstrated that the Bloch curve for atomic stopping powers (Whaling, 1958) applies to lithium. The target thicknesses are then 12.5 ± 3.6 kev for 2.7-Mev protons, and 54 ± 14 kev for 8.0-Mev He^3; the correction to the Q-value is 19 ± 5 kev. The resulting Q is -5.321 ± 0.010 Mev.

Three sources of error in the incident energies that may contribute errors to the Q-value are analyzing-magnet slit widths, linearity, and hysteresis.

The 90° magnetic analyzer is a 34-inch radius, uniform-field device, with beam-defining slits placed at the conjugate focal points $34\frac{1}{2}$ inches from the entrance and exit faces of the magnet (Pearson, 1963). Let E be the energy of a beam passing midway between both

sets of beam-defining slits. If the uncertainties in beam position are $\pm \delta X_1/2$ and $\pm \delta X_2/2$ at the entrance and exit slits, respectively, then the beam energy is defined to a precision $E \pm \delta E$, where

$$\delta E = \frac{E}{2R} \sqrt{\delta X_1^2 + \delta X_2^2} \quad .$$

R is the magnet radius of curvature. Both sets of slits were set to a width of 0.2 inches for all runs. The beam definition is considerably better than that calculated from the full slit width, because the beam must be steered so that nearly all of it passes through both slits. Since the beam diameter is about 0.1 inch, the core of the beam can wander only about 0.1 inch within the slits. δX_1 and δX_2 may therefore each be taken as 0.1 inch. The incident beam uncertainties are δE = 16.6 kev for the He^3 beam, and 5.6 kev for the proton beam. The error contribution to the Q-value is 13 kev.

The magnetic field is measured by a nuclear magnetic resonance probe. The beam energy is related to the n. m. r. frequency by the expression

$$E = K \frac{m_p}{m} q^2 \left(1 - \frac{E}{2mc^2}\right) f^2 \quad , \text{ where}$$

K = analyzer calibration constant;

m_p = proton mass;

m = ion mass;

q = ion charge in units of electronic charge; and

f = n. m. r. frequency

Fisher and Whaling (1964) have shown that K is constant to 1 part in 3000 over a range of magnetic field settings corresponding to an energy range of 2.5 to 10 Mev for a doubly-charged alpha beam. A measurement of the calibration constant performed shortly after the work reported here gave $K = (19885 \pm 6) \times 10^{-6}$ Mev/Mc^2 (McNally, 1963). The Q-value error introduced by the calibration-constant error is less than 2 kev, which may be neglected in comparison with the slit-width error.

The value given for the analyzer calibration constant assumes that the magnet current has been brought up to its correct value from zero. Fisher and Whaling (1963a) found that an error of 1 part in 1200 in energy may occur if the magnet current is reached from above. The Q-value error due to the effects of magnet hysteresis in setting the energy for the proton run is only 1.2 kev, which may be neglected. The current was reached from below for the He^3 run.

Uncertainties in the masses entering the computations (n, p, He^3, Li^7, Be^7) were neglected, since all of them are believed known to 1.1 kev or better (Everling et al., 1960). The uncertainty in the B^9 ground-state mass, which enters only in converting Q-values to excitation energies, is 1.8 kev, and may also be neglected.

The final Q-value is -5.321 ± 0.016 Mev. The excitation energy of the state is 14.668 ± 0.016 Mev. Several runs at 8.7-Mev incident energy give a Q-value consistent with that found from the 8.0-Mev run, although the uncertainty is about twice as large in each case. A repeat of the calibration spectrum (Figure 25), taken after several intervening $Li^7(p,n)Be^7$ runs at different incident energies, provides good evidence for the reproducibility of the results. The difference in the $(\chi_\gamma - \chi_n)$ values for the two spectra is well within the assumed half-channel uncertainty.

Although the width of the neutron peak in Figure 23 is significantly greater than the width of the gamma peak, it is possible to account for all of the excess width without having to assign an intrinsic width to the level. The contributions to the total observed width are the detector resolution (2.4 ± 0.5 channels), the beam burst duration (1.8 ± 0.2 channels), the target thickness (2.9 ± 0.7 channels), and the intrinsic level width. If the level is sharp, the total width w_o of the group should be 4.24 ± 0.6 channels; the observed width w is 4.2 ± 0.7 channels. An upper limit for the intrinsic level width may be estimated by finding the intrinsic width necessary to raise w to a value such that the error in w does not overlap with the error in w_o. The resulting upper limit for the width of the 14.67-Mev level is 45 kev.

An angular distribution of the neutrons to the 14.67-Mev level at 8.7-Mev incident energy is shown in Figure 27. Figures 13-16 are two examples of the spectra from which the angular distribution was taken. The dashed lines under the peaks in Figures 14 and 16 illustrate the method chosen to subtract the continuum. The errors attached to the angular-distribution points are due almost entirely to the continuum subtraction. The ratio of the cross section for neutron production in the forward hemisphere (c. m.) to the differential cross section at 0° c. m. is found by integrating the angular distribution. The result is

$$\frac{\sigma(0^\circ \text{ to } 90^\circ, \text{ c. m.})}{d\sigma/d\Omega(0^\circ, \text{ c. m.})} = 6.4 \pm 0.9 \text{ sr} .$$

Absolute differential cross sections for the $Li^7(He^3, n)B^9$ reaction are found by comparing the neutron yield with the yield from the $Li^7(p, n)Be^7$ (ground state) reaction, using the same target and geometry, and at the same neutron energy. At 8.7-Mev incident He^3 energy, the neutrons from the 14.67-Mev B^9 state have an energy of 1.75 Mev at 0°; the corresponding incident proton energy is 3.434 Mev. A typical pair of spectra is shown in Figures 9 and 28. Comparison of nine different pairs yields

$$\frac{d\sigma/d\Omega(B^9, 0°, \text{lab})}{d\sigma/d\Omega(Be^7, 0°, \text{lab})} = 0.0340 \pm 0.0045 .$$

Using a value of 48 mb/sr for the Be^7 cross section (Bevington et al., 1961) and converting the result to the center-of-mass system gives

$$d\sigma/d\Omega(B^9, 0°, \text{c.m.}) = 0.62 \pm 0.08 \text{ mb/sr.}$$

The forward-hemisphere cross section is then

$$\sigma(0° \text{ to } 90°, \text{ c.m.}) = 4.0 \pm 0.8 \text{ mb.}$$

Since the angular distribution shows no appreciable structure in the forward hemisphere, it may be reasonable to assume that it is symmetrical about 90° c. m. The total cross section would be 8 mb. The effects of possible back-angle peaking on the total cross section would be diminished by the sin θ weighting factor which enters in integrating differential yields to obtain a total yield.

The 0° differential cross section at 8.0-Mev incident energy is found from the spectra of Figures 24 and 25, by using the same procedure as for the 8.7-Mev data. The results are

$$\frac{d\sigma/d\Omega(B^9, 0°, \text{lab})}{d\sigma/d\Omega(Be^7, 0°, \text{lab})} = 0.034 \pm 0.005, \text{ and}$$

$$d\sigma/d\Omega(B^9, 0°, c.m.) = 0.49 \pm 0.08 \text{ mb/sr.}$$

4. The 14.0-Mev Level

The neutron group corresponding to the 14.0-Mev B^9 level is difficult to see in counts-vs.-time spectra because it is broad and of low intensity, and especially because it lies on an intense continuum with a large slope. When the continuum is smoothed by converting the counts-vs.-time spectra to counts-vs.-energy spectra, the neutron group stands out clearly. Since the group appears consistently in all spectra with sufficient time resolution to resolve it, and since its energy shifts appropriately with changes in angle and bombarding energy, there is little doubt that it corresponds to structure in B^9.

Figures 23-25 provide the best information about the position and width of the 14.0-Mev level, as well as the 14.67-Mev level. Because the width of the state is several hundred kev, no attempt was made to determine the level position precisely by direct comparison with a $Li^7(p,n)Be^7$ peak having the same neutron energy. The B^9 spectrum is calibrated near the 14.67-Mev peak by the Be^7 spectrum of Figure 25, and a time scale is then generated from a random time spectrum (Figure 26), as explained in Appendix A, Section 4. The center of the group is taken as $\chi_n = 44 \pm 1.5$, and

the target-thickness correction is made in the manner described in Section 3 of this part. The results are $Q = -4.66 \pm 0.07$ Mev, and $E_x = 14.01 \pm 0.07$ Mev.

The level-width estimate is subject to considerable error from the continuum subtraction. The choice made is indicated by the dashed line in Figure 24. The full width at half maximum of the group is taken as $\Delta E_{II} = 575 \pm 150$ kev. The error includes the effects of a 200-count error in choosing the continuum level, and a 100-kev error in estimating the width of the group at a given continuum level. Contributions to the observed group width, other than the intrinsic width, are the target thickness (40 kev), the detector resolution (130 kev), and the beam burst duration (120 kev). Upon extracting these, the intrinsic group width becomes $\Delta E_n = 545 \pm 150$ kev, and the state width is $\Gamma = 390 \pm 110$ kev.

5. The 12.06-Mev Level

Although the neutron group corresponding to the 12.06-Mev level is the most prominent feature of all the B^9 spectra, it is the most difficult to interpret, because of its large width and because of the shape of the underlying continuum. The data must be examined in the counts-vs.-energy presentation.

Figures 14, 20, and 24 show the tendency of the continuum to increase toward low neutron energies. In all spectra the

continuum appears to change intensity rapidly in the region of the group from the 12.06-Mev state. The continuum subtraction strongly affects the measurement of the level width, and, to a lesser extent, the position of the level. In all cases, the attempt was made to fit the continuum smoothly to the remainder of the spectrum at the high- and low-energy sides of the group; to avoid sharp changes in the continuum slope; and to make the shape of the neutron group as symmetric as possible. A typical estimate of the continuum intensity is indicated by the dashed line in Figure 24.

Fisher and Whaling (1963) have observed a level of 700-kev width at an excitation energy of 11.62 Mev in the $B^{10}(He^3,\alpha)B^9$ reaction. A neutron group corresponding to such a level should distort the shape of the high-energy side of the group corresponding to the 12.06-Mev state, even if it is not resolved. No structure around 11.6-Mev excitation in B^9 appears in any of the spectra, although a broad, weakly excited group appearing on the high-energy side of the observed group might contribute to its apparent asymmetry. Since there is no definite evidence for a second level in the spectra, it will be assumed that the structure near 12-Mev excitation corresponds to a single B^9 level.

An attempt was made to locate the peak of the group accurately by using a low bombarding energy and maximizing the resolution. A spectrum taken at 6.25-Mev incident energy and at 45°

laboratory angle is shown in Figures 29 and 30. The spectrum was calibrated at 1.55-Mev neutron energy by the $Li^7(p,n)Be^7$ spectrum of Figure 31, with identical target and geometry. The channel assignment for the peak is $\chi_n = 39.5 \pm 1$, and the Q, uncorrected for target thickness, is -2.756 ± 0.060 Mev. The target thickness, estimated from the ground-state yield in Figure 31, is 160 kev for 6.25-Mev He^3; the correction to the Q is 43 kev. The Q-value becomes -2.71 ± 0.06 Mev.

Results taken from two spectra at 6.25-Mev bombarding energy and at 0° are consistent with the 45° results, although the resolution in each case is only about half as good as for the 45° run. The excitation energies calculated from the two spectra are 12.03 ± 0.1 and 12.08 ± 0.1 Mev. Comparison of the neutron energies at 0° and 45° yields a residual nucleus mass of 9 ± 1.

Excitation energies computed from a number of counts-vs.-energy spectra at higher bombarding energies show a tendency to rise with increasing incident energy. In the 8.0-Mev spectrum (Figure 24), for example, the apparent excitation energy is 12.3 ± 0.2 Mev. The increase can be attributed to a distortion of the shape of the group that occurs when the resolution is poor, the energy per channel is changing rapidly across the group, and there is a sloping continuum under the group. A similar shift has been seen in the neutron group corresponding to the first excited Ne^{18}

state in an 8.7-Mev spectrum in which an oxygen impurity was deliberately introduced. The group appears about 10 channels lower than the group from the 12.1-Mev B^9 state. The peak of the Ne^{18} group occurs at the correct position in the time spectrum, but appears shifted toward lower neutron energy by about a channel in the counts-vs.-energy spectrum. The excitation energy computed from the 6.25-Mev runs should be reliable, since the group width is several times the resolution width, and the peak is very well defined. The excitation energy will be taken as 12.06 ± 0.06 Mev.

Level widths extracted from four 0° spectra at 6.25, 7.14, 8.0, and 8.7-Mev bombarding energy show surprising consistency, in spite of the difficulty of subtracting the continuum. After the spectrometer resolution has been removed, all four values are very close to $\Gamma = 800 \pm 200$ kev. In each case, the error was computed by estimating upper and lower limits on the continuum level, beyond which either the continuum shape acquires an unlikely variation in slope, or the level becomes unreasonably asymmetric.

6. The 16.02-Mev Level

The neutron group corresponding to the 16.02-Mev level is clearly visible only in spectra at 10.5-Mev incident energy and above. At 10 Mev (450 kev above threshold), the group appears very weakly as a distortion of the continuum. The best values for the

Q and the level width are found from the 10.5-Mev spectrum of Figure 10, which was calibrated at the position of the neutron group by the $Li^7(p,n)Be^7$ spectrum of Figure 9. The target and geometry were identical for the spectra of Figures 9 and 10.

The Q-value is extracted by the same procedure as for the 14.67-Mev state. Assigning $\chi_n = 35.5 \pm 0.5$ to the neutron peak position, and estimating a target thickness of 54 ± 14 kev for 10.5-Mev He^3 from Figure 9, the Q is -6.675 ± 0.025 Mev, and the excitation energy is 16.022 ± 0.025 Mev.

The extrapolation of the continuum under the group is straightforward. Examination of the data in either the counts-vs.-energy or counts-vs.-time presentation yields a value for the group width of 5.1 ± 0.3 channels. The width of the neutron group in Figure 9 is essentially the same as that of the gamma peak. Accordingly, the resolution for the neutron group in Figure 10 is taken to be the same as for the gamma peak, or 2.8 ± 0.2 channels. The level width, after correction for target thickness, is $\Gamma = 180 \pm 16$ kev.

A 0° differential cross section at 10.5-Mev incident energy is obtained from the spectra of Figures 9 and 10, and from two similar pairs. The average of the values found from the three pairs is

$$\frac{d\sigma/d\Omega(B^9, 0°, \text{lab})}{d\sigma/d\Omega(Be^7, 0°, \text{lab})} = 0.0169 \pm 0.0035 .$$

Using Bevington's (1961) cross section of 48 mb/sr (0°, lab, $E_p = 3.434$ Mev) for the $Li^7(p,n)Be^7$ reaction, and converting to the center of mass system,

$$d\sigma/d\Omega(B^9, 0°, \text{c.m.}) = 0.275 \pm 0.060 \text{ mb/sr.}$$

7. The Continuum

It is necessary to examine the sources of continuum neutrons, in order to ensure that no broad peaks may occur in the continuum that can be confused with B^9 groups. Energies of the neutrons may extend from zero up to the maximum energy allowed by the $Li^7 + He^3 \rightarrow 2\alpha + p + n$ four-particle breakup (see Figure 3). The spectrometer resolution is insufficient to separate the four-body breakup endpoint from the B^9 ground state and from the endpoint of the three-body reaction $Li^7 + He^3 \rightarrow Be^8 + p + n$. The maximum-energy endpoint of the neutron spectra is always well defined, and is always consistent with the above-mentioned reactions. The intensity of the continuum appears to increase toward lower neutron energies, and to level off near the lowest energies observed (about 1 Mev).

Peaks in the continuum may be formed under certain conditions if neutrons are liberated in the second stage of a multistage decay sequence, such as $Li^7 + He^3 \rightarrow Be^{9*} + p \rightarrow Be^8 + n + p \rightarrow 2\alpha + n + p$. Clear evidence for similar processes has been found in other reactions. For example, Jarmie, Silbert, and Smith (1961) have observed well-defined proton groups from the reaction $N^{14} + t \rightarrow O^{16}$ (E_x = 16.22 Mev) + n $\rightarrow N^{15} + p + n$.

The conditions necessary for formation of a continuum peak at low neutron energies in the $Li^7 + He^3$ reactions are low center-of-mass velocity, a high positive Q-value for the first-stage reaction, and a low Q for the second-stage breakup which emits the neutron. The sequence most nearly fulfilling these conditions is the process

$$Li^7 + He^3 \rightarrow Be^9 \ (E_x = 2.43 \text{ Mev}) + p; \ Q = 8.77 \text{ Mev}$$
$$\hookrightarrow Be^8 + n; \ Q = 0.765 \text{ Mev}.$$

A simple kinematics calculation shows that the upper- and lower-energy endpoints for a bombarding energy of 8.7 Mev are 3.03 and 0.86 Mev at 0°. No clearly identifiable broad structure is seen in Figure 14 having the calculated endpoints, although the process probably contributes to the continuum. Similarly, no structure is seen in Figure 21 having the calculated endpoints 2.89 and 0.87 Mev. If Be^9 were formed in a state close to the neutron threshold at

1.665 Mev, the upper endpoint would always be in the unobserved region below 1 Mev. Since all of the other possible reactions have even more widely separated endpoints, it seems reasonable to conclude that all of the peaks in the spectra are due to the $Li^7(He^3, n)B^9$ primary reaction.

8. Target Impurities

Very little difficulty is caused by target contaminants. Narrow groups produced by target contamination cannot be confused with the relatively wide groups from the 12.06- and 14.0-Mev B^9 levels. On the other hand, the shapes of wide groups could be distorted by weak, narrow groups lying on top of them. Impurities of mass 12 or greater cannot produce neutron groups that may be mistaken for B^9 levels, because the energy of the impurity groups will not shift enough when the angle of observation is changed. The effects of possible contaminants among the light nuclei are considered below.

Li^6. The purity (over 99%) of the Li^7 used for the target should guarantee the absence of peaks from Li^6. The $Li^6(He^3, n)B^8$ reaction has been investigated at a bombarding energy near 8 Mev (Dietrich, Honsaker, and Davies, 1963). Strong, well-defined neutron groups of similar intensity are seen corresponding to the known ground and first excited B^8 states, and to a previously un-

reported level at 2.17 Mev. There is no evidence for B^8 peaks in any of the B^9 spectra. For example, the neutron group from the 2.17-Mev B^8 level would appear at $\chi_n = 50$ in Figure 23.

Be^9, B^{10}, and B^{11}. These unlikely candidates are eliminated by the fact that the Q-values for formation of the ground states of C^{11}, N^{12}, and N^{13} are positive, and therefore a number of narrow states should appear in the B^9 spectra if impurities are present. No groups are seen corresponding to known levels of C^{11}, N^{12}, or N^{13}.

C^{12}. The impurity groups from C^{12} should be readily identified, since the $C^{12}(He^3,n)O^{14}$ ground state Q is -1.148 Mev, and the first excited state of O^{14} is at $E_x = 5.91$ Mev. The ground-state neutron group should always appear at a neutron energy 1 or 2 Mev higher than the $E_x = 12.06$-Mev B^9 group. Occasionally a high point is observed at the expected position, as at $\chi_n = 69$ in Figure 23, but no distinct peak was ever seen in the foreground runs. There is likewise no evidence for an impurity peak from the 5.91-Mev O^{14} state, which should appear between the peaks from the 16.02- and 14.67-Mev B^9 states ($\chi_n = 41$ in Figure 10).

N^{14}. At present there is no accurate information on the mass of F^{16}. The ground-state Q-value for the $N^{14}(He^3,n)F^{16}$ reaction is expected to be around -1.2 Mev, based on the known Q

for $N^{14}(t,p)N^{16}$. A preliminary investigation of the $N^{14}(He^3,n)F^{16}$ reaction by Ajzenberg-Selove, Zafiratos, and Dietrich (1963), showed a group of weakly excited states analogous to the first four N^{16} states clustered around an intense carbon impurity group. It appeared that the $N^{14}(He^3,n)F^{16}$ cross section was much smaller than the $C^{12}(He^3,n)O^{14}$ cross section. Since the carbon impurity groups are weak in the B^9 spectra, the nitrogen groups should be negligible.

O^{16}. Oxygen is the most troublesome contaminant because the $O^{16}(He^3,n)Ne^{18}$ ground and first excited state neutron groups fall near the broad 12.06- and 14.0-Mev B^9 groups. When target preparation was careless, a distinct distortion appeared on the high neutron energy side of the 12.06-Mev group. No distortion occurred when the lithium was cleaned carefully and the evaporation furnace was allowed to reach its base pressure before making the target. An occasional high point was noticed near the 14.0-Mev B^9 level at a position corresponding to formation of Ne^{18} in its first excited state at 1.88 Mev. High points are seen in Figures 13 and 15 at $\chi_n = 51$ which may be weak Ne^{18} groups.

Other Impurities. C^{13}, N^{15}, O^{17}, and O^{18} may be eliminated by their low isotopic abundance, since no strong contamination is observed from C^{12}, N^{14}, and O^{16}. The $F^{19}(He^3,n)Na^{21}$ reaction

has a high Q-value, and should excite many states, none of which are seen.

IV. DISCUSSION OF RESULTS

1. Summary of Other Recent Experimental Results

$\underline{Li^7(t,p)Li^9}$. Middleton and Pullen (1964) have bombarded Li^7 targets with an 11.28-Mev triton beam from the Aldermaston tandem accelerator. They observed the ground state of Li^9 ($Q = -2.397 \pm 0.020$ Mev), and an excited state at $E_x = 2.691 \pm 0.005$ Mev. No other excited states were seen up to $E_x = 4$ Mev. The ground-state angular distribution exhibits a pronounced forward peak which can be fitted roughly with a plane-wave stripping calculation involving $L = 0$ and $L = 2$ orbital angular momenta. No absolute cross sections were measured. At a laboratory angle of 27.5°, the yield of the excited state is about one-third that of the ground state.

$\underline{Li^7(He^3,p)Be^9}$. Lynch, Griffiths, and Lauritsen (1964) have examined the proton yield from the $Li^7(He^3,p)Be^9$ reaction at incident energies up to 10 Mev, using the ONR-CIT tandem accelerator and the 24-inch magnetic spectrometer. A narrow Be^9 state was found at $E_x = 14.392 \pm 0.005$ Mev, having a width of less than 5 kev. An angular distribution at 10-Mev incident energy is nearly symmetric about 90° center-of-mass angle, having maxima at 40° and 150°. The peak-to-valley ratio is about 2. Total cross sections are $7.5 \pm \frac{4}{2}$ mb at $E(He^3) = 7.5$ Mev, and $10 \pm \frac{5}{2}$ mb at $E(He^3) = 10$ Mev. Because of the narrow width of the level, and because of the close correspondence

between its mass and that of the Li^9 ground state (see Figure 2), Lynch et al. argue that the level probably has isospin 3/2. Cocke (1964), continuing the above work, has found preliminary evidence for Be^9 groups at E_x = 11.26, 11.79, and 13.73 Mev, with widths of roughly 500 kev.

Gamma radiation from $Li^7 + He^3$. Griffiths (1964) has observed high-energy gamma radiation from He^3 bombardment of Li^7. Two distinct thresholds can be seen in the gamma excitation function near incident energies of 4.56 and 7.60 Mev, which correspond to thresholds for production of the 14.39-Mev Be^9 state and the 14.67-Mev B^9 state, respectively. Gamma transitions were observed to the ground states of Be^9 and B^9 ($E_\gamma \approx 14.5$ Mev), and to the excited states at E_x = 2.43 Mev in Be^9 and E_x = 2.34 Mev in B^9 ($E_\gamma \approx 12$ Mev). Apart from the two thresholds, the excitation function shows a smooth behavior with energy up to $E(He^3)$ = 10 Mev. Above the 7.60-Mev threshold, the gamma yield appears to have the $(E-E_{thresh})^{\frac{1}{2}}$ energy dependence characteristic of s-wave neutron production in the $Li^7(He^3,n)B^9$ reaction. For the 14.39-Mev Be^9 state, there are 0.056 gamma rays per proton exciting the state, and the ratio of 12- to 14.5-Mev gammas is about 1.5. The gamma radiation is probably M1, which is consistent with a $3/2^-$ spin and parity assignment for the state. From the 18-ev radiation width measured by Edge and Peterson (1962) by inelastic electron scattering on Be^9, Griffiths has

inferred that the total width of the state is probably less than 1 kev. At 10-Mev incident energy, the ratio of the gamma ray intensity from the 14.39-Mev Be^9 state to that from the 14.67-Mev B^9 state is about 1.8.

$Li^7(He^3,n)B^9$. Duggan (1962) has investigated the $Li^7(He^3,n)B^9$ reaction at bombarding energies up to 2.7 Mev, and finds no evidence for sharp B^9 levels from about 3- to 8-Mev excitation, although the shape of the neutron continuum is suggestive of a broad level near 7-Mev excitation. Duggan's results are consistent with the work presented in this thesis.

$B^{10}(He^3,\alpha)B^9$. Fisher and Whaling (1963) have examined the alpha spectrum from He^3 bombardment of B^{10} at an incident energy of 10 Mev, using the ONR-CIT tandem accelerator and 24-inch magnetic spectrometer. Although it should have been possible to observe B^9 states up to E_x = 17 Mev, the only states resolved were the ground state, the 2.34-Mev state, and a previously unreported state at 11.62 Mev with width 700 kev. Since the $B^{10}(He^3,\alpha)B^9$ reaction should be capable of forming only $T = \frac{1}{2}$ states, it is not surprising that the 14.67-Mev B^9 level was not excited; but it is not clear why none of the other levels found in the $Li^7(He^3,n)B^9$ reaction was seen.

2. Discussion

Intermediate-coupling shell model calculations (Kurath, 1956) for the mass-nine nuclei predict a $3/2^-$, $T = 3/2$ level near 15-Mev excitation, which probably corresponds to the levels at 14.39 Mev in

Be^9 and 14.67 Mev in B^9. The position of the T = 3/2 level is not strongly dependent upon the value of the intermediate coupling parameter a/K. There is a set of T = $\frac{1}{2}$ levels in the 10- to 16-Mev region which corresponds to a ^4D multiplet in the LS-coupling limit, but there is no obvious correlation between these levels and the observed ones. Kurath points out that calculations of highly excited levels of a given isospin are unreliable, because effects of the 2s and 1d shells have not been taken into account.

In view of the fact that the ground state of B^9 is unbound to proton emission, the highly excited levels are surprisingly narrow. An isotopic-spin selection rule applies to the decay of B^9 levels below the threshold for breakup into Be^8(16.62 Mev; T = 1) + p at E_x =16.43 Mev; heavy-particle emission from T = 3/2 levels should be forbidden if isospin is conserved. The very narrow width of the 14.67-Mev level suggests the operation of the isospin selection rule, and consequently a T = 3/2 assignment for the state. Although the upper limit placed on the width of the state by the $Li^7(He^3, n)B^9$ reaction is 45 kev, Griffiths' gamma-ray work indicates that the level is much narrower than the experimental limit. If the total cross section at 8.7-Mev incident energy for formation of the 14.67-Mev B^9 state (8 mb) is extrapolated to 10 Mev by assuming an $(E-E_{thresh})^{\frac{1}{2}}$ energy dependence for the excitation function, the cross section becomes 12 mb, which is comparable to the cross section for formation of the 14.39-Mev Be^9 state in the $Li^7(He^3, p)Be^9$ reaction at 10-Mev incident energy. Since the gamma yield at 10-Mev incident energy from the Be^9 state is nearly

twice as large as for the B^9 state, it would be inferred that the width of the B^9 state is about twice that of the Be^9 state, if the gamma-decay rates are assumed to be the same in the two cases. Following Griffiths' argument for the width of the Be^9 state, the width of the B^9 state would be less than 2 kev.

A relation between the cross sections for the processes $Li^7(t,p)Li^9$, $Li^7(He^3,p)Be^9$, and $Li^7(He^3,n)B^9$ may be found by assuming charge independence of the nuclear forces causing the reactions. The cross sections are proportional to the absolute squares of the amplitudes A, given by

$$A(T_i T_{3i} t_i t_{3i} \rightarrow T_f T_{3f} t_f t_{3f}) = \sum_{\tau} (T_i T_{3i} t_i t_{3i} | \tau, T_{3i}+t_{3i})(T_f T_{3f} t_f t_{3f} | \tau, T_{3f}+t_{3f})\, a_\tau . \qquad (1)$$

T_i, T_{3i} and t_i, t_{3i} are the isospins and charge projections of the target and incident nuclei, respectively; T_f, T_{3f} and t_f, t_{3f} are the same quantities referred to the residual and observed nuclei. The sum runs over the intermediate isospin values τ which can be formed from both the initial and final systems. The amplitudes a_τ are independent of all charge-projection quantum numbers.

For $T = 3/2$ states in the residual nucleus, only the $\tau = 1$ channel is available, and the cross sections are proportional to the following:

$$|A|^2 = \tfrac{3}{4}|a_1|^2, \ Li^7(t,p)Li^9 ; \quad \tfrac{1}{4}|a_1|^2, \ Li^7(He^3,p)Be^9 ; \quad \tfrac{1}{4}|a_1|^2, \ Li^7(He^3,n)B^9 . \qquad (2)$$

For $T = \frac{1}{2}$ states in the residual nucleus, both $\tau = 0$ and $\tau = 1$ channels may contribute:

$$|A|^2 = \tfrac{1}{4}(|a_o|^2 + |a_1|^2 + 2\mathrm{Re}\ a_o a_1^*),\ \mathrm{Li}^7(\mathrm{He}^3,p)\mathrm{Be}^9\ ;$$
$$= \tfrac{1}{4}(|a_o|^2 + |a_1|^2 - 2\mathrm{Re}\ a_o a_1^*),\ \mathrm{Li}^7(\mathrm{He}^3,n)\mathrm{B}^9\ . \qquad (3)$$

Caution must be exercised in using the above relations to compare the experimental results for different reactions. If the reaction mechanism is strongly dependent upon the reaction Q-value and upon the incoming- and outgoing-channel energies, the differing coulomb energies of the nuclei may destroy the significance of the comparison. Coulomb effects in the incoming and outgoing channels may be partially removed by dividing the measured cross sections by appropriate transmission coefficients.

The forward-peaked angular distribution of the ground-state protons in the $\mathrm{Li}^7(t,p)\mathrm{Li}^9$ reaction suggests that the reaction mechanism is probably different from that operating in the $\mathrm{Li}^7(\mathrm{He}^3,p)\mathrm{Be}^9$ and $\mathrm{Li}^7(\mathrm{He}^3,n)\mathrm{B}^9$ reactions, and that a detailed comparison of all three reactions is not fruitful. Nevertheless, if the 14.67-Mev B^9 level is assumed to have isospin 3/2, the $\mathrm{Li}^7(t,p)\mathrm{Li}^9$ results indicate that the next $T = 3/2$ B^9 level should lie near 17.3 Mev, and that the 16.02-Mev level has isospin $\frac{1}{2}$. Levels have been observed in B^9 at 17.19- and 17.63-Mev excitation (see Figure 1), but it is not clear whether either level is the analogue of the 2.69-Mev Li^9 state.

Agreement between the results obtained from the $Li^7(He^3,p)Be^9$ and $Li^7(He^3,n)B^9$ reactions is reasonably good, because the incoming channels are identical, and because the same range of bombarding energies was employed. The smooth behavior of Griffiths' gamma excitation function suggests that the reaction mechanism may not be changing rapidly in the region of 7.5- to 10-Mev incident energy. Cross sections for formation of the 14.39-Mev level in the $Li^7(He^3,p)Be^9$ reaction were found to be 7.5 and 10 mb at 7.5- and 10-Mev incident energy, respectively; the cross section for formation of the analogous B^9 level at 8.7-Mev incident energy is 8 mb (see p. 28). According to (2), these cross sections should be equal, if corrections are made for the differing transmission coefficients in the outgoing channels. The shape of the gamma excitation function suggests the use of s-wave transmission coefficients. The transmission coefficients were computed from the graphs prepared by Sharp, Gove, and Paul (1955), and are defined by expression (5.5), Chapter VIII, Blatt and Weisskopf (1952). For a nuclear radius of 3.5×10^{-13} cm, the s-wave transmission coefficients are 0.54 and 0.71 for the (He^3,p) case at 7.5- and 10-Mev incident energy, respectively; and 0.52 for the (He^3,n) reaction at 8.7 Mev. Division of the cross sections by the transmission coefficients yields 13.9 mb at 7.5 Mev and 14.1 mb at 10 Mev for (He^3,p), and 15.5 mb at 8.7

Mev for (He^3, n). The agreement is well within the uncertainties in the experimental values, and remains good even for nuclear radii greater than 6×10^{-13} cm.

APPENDIX A. DATA ANALYSIS

1. Introduction

The multichannel analyzer in which the data are stored records counts as a function of channel number. If the time-to-pulse-height converter and inverting amplifier were completely linear, the channel number would be a linear function of flight time, and the data would be stored as counts per time interval. Broad neutron groups and prominent continuum spectra are often difficult to interpret from data presented in this form, as the shapes of such structures may be distorted by exhibiting them as functions of flight time rather than of neutron energy.

This appendix describes simple methods of extracting information from the data, and then describes a computer program in which the data are converted to the counts-vs.-energy presentation, and in which time-to-pulse-height-converter nonlinearities are taken into account. The computer program is checked by comparing its results with those of the simple calculations in specific cases.

2. Simple Analysis

The assumption that channel number is linearly related to flight time may be expressed as

$$t = \tau_c (\chi_o - \chi) , \qquad (1)$$

where t is the flight time, τ_c is the time per channel, χ_o is the channel corresponding to zero flight time, and χ is the channel corresponding to the flight time t.

τ_c may be determined from a spectrum with two known points. It is dependent only upon the amplitude of the time-to-pulse-height-converter output, the gain of the inverter amplifier, and the settings of the multichannel analyzer. Since these units have proven stable over a period of days after initial warm-up, τ_c need be determined only by an occasional run.

The zero-time channel χ_o is dependent upon incident particle energy and stop-pulse phasing, and must be redetermined whenever a change is made in the machine energy or the r. f. electronics. χ_o may easily be found if a spectrum has a gamma-ray peak:

$$\chi_o = \chi_\gamma + \frac{d}{c\,\tau_c} , \qquad (2)$$

where χ_γ is the channel assigned to the gamma peak, and d is the flight path.

The nonrelativistic relation between flight time and neutron energy is

$$\sqrt{E_n} = K \frac{d}{t} . \qquad (3)$$

If E_n is measured by Mev, d in meters, and t in ns, then $\mathcal{K} = 72.3$.

Differentiating (3) gives expressions for the resolution,

$$\delta E_n / E_n = 2(\delta t/t), \tag{4}$$

and the neutron energy per channel,

$$\delta E_n / \delta \chi = 2E_n/(\chi_o - \chi). \tag{5}$$

The yield per channel $y(\chi)$ is related to the yield per unit energy $y(E_n)$ by the condition

$$y(\chi)\, \delta \chi = y(E_n)\, \delta E_n . \tag{6}$$

Then

$$y(E_n) = \tfrac{1}{2} \left(\frac{\tau_c}{\mathcal{K} d} \right)^2 (\chi_o - \chi)^3\, y(\chi), \tag{7}$$

and

$$y(\chi) - 2 \frac{\tau_c}{\mathcal{K} d} E_n^{3/2}\, y(E_n) . \tag{8}$$

The time-independent background underlying most time spectra must be subtracted before the time-energy conversion, since a smooth background will be sharply peaked toward low energies by the $(\chi_o - \chi)^3$ factor in (7). Therefore, $y(\chi)$ in (7) and (8) should be taken as

$$y(\chi) = y_o(\chi) - y_B \,, \tag{9}$$

where $y_o(\chi)$ is the total number of counts in channel χ, and y_B is the time-independent background counting rate per channel.

3. Sample Calculations

The $Li^7(He^3, n)B^9$ spectrum of Figure 23 was taken with a flight path of 2.105 m and at an angle of 0°. Immediately thereafter, the $Li^7(p, n)Be^7$ spectrum of Figure 25 was run with the same target and geometry.

τ_c is found from Figure 25 and the well-known Q of the $Li^7(p, n)Be^7$ reaction. At 2.7-Mev incident proton energy, the energy of the neutrons corresponding to the Be^7 ground state is 0.997 Mev. The flight time of the neutrons is 152.4 ns, and the gamma flight time is 7.0 ns. Assigning $\chi = 18.5$ to the neutron group in Figure 25 and $\chi_\gamma = 93.8$ to the gamma peak, $\tau_c = 1.931$ ns/channel. In Figure 23, the gamma peak appears at $\chi_\gamma = 97.0$, and we find $\chi_o = 100.64$. The energies of the neutron groups can now be found. Table II gives the neutron energy, resolution, and energy per channel at four significant points of the spectrum. The next two entries in the table give the Q and residual-nucleus excitation energy, assuming that the neutrons are produced in the $Li^7(He^3, n)B^9$ reaction. The time-independent background counting

rate y_B can be estimated by averaging several channels between the highest energy neutrons and the gamma peak. Averaging channels 85 through 90 in Figure 23 gives $y_B = 902$. The seventh and eighth columns of Table II show the counts-vs.-time and counts-vs.-energy yields. In the last column the counts-vs.-energy yields have been divided by the detector efficiency calculated from (1) and (2) of Section 7, Part II, with $E_o = 0.45$ Mev.

4. Computer Analysis

An IBM 7090 FORTRAN computer program was written to facilitate the conversion of time spectra to energy spectra, and to determine accurately the neutron energy corresponding to each channel.

Relativistic calculations are used throughout the program.

Figure 26 shows a random time spectrum, in which a Cs^{137} source provides detector pulses, and stop pulses are generated in exactly the same manner as if a neutron spectrum were being run. Since the Cs^{137} gamma rays are emitted at randomly distributed times, the counting rate in each channel is proportional to the time interval represented by that channel. The random time spectrum shows significant deviations from the flat spectrum expected if the linearity assumption of Section 2 were valid. The computer

program generates an accurate time scale from a random time spectrum by assigning to each channel χ_n a time T_n according to the expression

$$T_n = \lambda \sum_{n+1}^{99} C_m , \qquad (10)$$

where C_m is the counting rate in channel χ_m of the random time spectrum. T_n is arbitrarily set to zero at the uppermost channel (channel 99). The proportionality constant λ must be determined from a known spectrum. Typically, a spectrum with a known neutron peak and a gamma peak is given to the computer, together with the approximate locations of the peaks and sufficient information to determine the neutron and gamma flight times. The program fits parabolas to the uppermost three points of the peaks to determine their centers, calculates the difference in flight times between the neutron and gamma peaks, and computes the quantities T_n.

The neutron energy scale for a data run is found from the T_n and from the position of the gamma peak. The gamma position may be specified, or may be computed by fitting a parabola to the three highest points of the gamma peak. If the masses of the incident and target nuclei are provided, the reaction Q is calculated for each channel.

The time-independent background correction for the time-to-energy yield conversion is accomplished by normalizing the random time spectrum to a portion of the data spectrum and subtracting it. The normalization factor is found by dividing the average yield between any two specified channels of the data spectrum by the average yield between the same two channels of the random time spectrum. The converted yield is corrected for detector sensitivity according to (1) and (2) of Section 7, Part II. Statistical errors in the original data and in the converted yield are computed and tabulated.

A useful feature of the program is the computation of errors in Q resulting from small variations in the input parameters. The data spectrum parameters are the incident energy, flight path, laboratory angle, and gamma peak channel. Changes in input parameters for the calibration spectrum also vary Q through their effect on the T_n. Errors in data spectrum Q-values are computed for small variations in incident energy, flight path, laboratory angle, gamma peak channel, and reaction Q for the calibration spectrum.

5. Sample Computer Calculations

Table III contains results of computer calculations for the spectrum of Figure 23. Figures 25 and 26 were taken as the

calibration and random time spectra, respectively.

The computer chose channels 18.50 and 93.88 for the peaks in the calibration spectrum, and calculated a time difference of 145.48 ns between them. Values of T_n generated from this calibration are shown in the second column of Table III. The position of the gamma peak in Figure 23 was found to be at $\chi_o = 97.02$. The corresponding point on the time scale is $T_n = 4.05$ ns. Neutron energies and Q-values (for the $Li^7(He^3, n)B^9$ reaction) are shown in the third and fourth columns of the table. The next column shows the converted yield. The time-independent background subtraction was found by normalizing the data and random time spectra at channels 85-90, and the detector sensitivity cutoff was taken as $E_o = 0.45$ Mev. A part of the converted spectrum is plotted in Figure 24.

Examples of the error calculations are shown in the last four columns of the table. The first of these columns gives the variation in Q produced by a variation in the incident proton energy for the calibration spectrum; the remaining columns refer to variations in Q produced by variations in incident energy, flight path, and gamma peak position for the data spectrum.

6. Discussion

Comparison of Tables II and III shows that the results of the computer calculations are in close agreement with those of the simple analysis.

The agreement on E_n is excellent at $\chi = 20$, since the time scale was calibrated at a nearby channel. The small, but significant, discrepancies at $\chi = 44$ and 61 show the effects of time scale nonlinearity at channels distant from the calibration point. The surprisingly good agreement at $\chi = 82$ is due to cancellation of the time scale nonlinearity error by the relativistic correction to the neutron energy, which amounts to about 500 kev.

The time scale nonlinearity introduces two sources of error into the converted yield $Y(E_n)$ computed by the simple methods. Expression (8) is correct even for a nonlinear time scale, if the average time per channel τ_c is replaced by the true time per channel $T_n - T_{n-1}$. Since the time per channel varies by several per cent over the spectrum, considerable error can be introduced by using τ_c in the conversion formula. Secondly, the time-independent background subtraction may be in error because the assumption that the background has the constant value y_B is not valid. At $\chi = 20$, the simple analysis overestimates the yield by about 10%, since the two sources of error are both significant and have the same sign.

APPENDIX B. BUNCHER PERFORMANCE

Fairly simple calculations of buncher performance may be made by assuming that the ion-source energy spread is small compared with the buncher energy modulation, that the required energy modulation is small relative to the source energy, and that the optical properties of the system are independent of energy over the range of energy modulation. The experimental results are in reasonable qualitative agreement with these calculations, even though none of the assumptions is strictly valid.

At a distance x from the outgoing end of the buncher cylinders, the current profile is

$$i(t) = \frac{i_o}{\left| 1 + \gamma q \frac{dV(t')}{dt'} \right|} , \qquad (1)$$

where i_o is the steady state current, and $i(t)$ is the instantaneous current with the buncher operating. γ is given by

$$\gamma = -\sqrt{2m}\ (\ell + x)\ E^{-3/2} , \qquad (2)$$

where E is the energy of the beam entering the buncher, m is the ion mass, and ℓ is the length of a buncher section. t' is the time at which particles arriving at x at time t entered the buncher.

t and t' are related by the expression

$$t = t' + \sqrt{\frac{m}{2E}}\ (x + 2\ell) + \gamma q V(t') \quad . \tag{3}$$

For a sinusoidal bunching waveform $V(t) = V_o \sin \omega t$,

$$\omega t = \omega t' + \alpha \sin \omega t' \text{ , and} \tag{4}$$

$$\frac{i(t)}{i_o} = \frac{1}{|1 + \alpha \cos \omega t'|} \quad , \tag{5}$$

where $\alpha = \omega \gamma q V_o$, and the term $\sqrt{\frac{m}{2E}}\ (x + 2\ell)$ in (3) has been dropped, since it merely shifts the phase at which bunching takes place. Bunching occurs when (5) is largest, and this condition clearly requires

$$|\alpha| = |\omega \gamma q V_o| = 1 \tag{6}$$

for bunching in a single peak.

Figure 6 is a graph of the relation (4) between ωt and $\omega t'$ for several values of α. For $\alpha > 1.0$, $\omega t'$ is a triple-valued function of ωt in a region around $\omega t = \pi$. In this region (5) must be replaced by a sum of three similar terms, one for each of the values of $\omega t'$ corresponding to ωt. A full cycle of the current profile is shown in Figures 7 and 8 for $\alpha = 0$, 0.8, 1.0, and 1.5. A horizontal line at $i/i_o = 1$ represents the unbunched beam ($\alpha = 0$).

The optimum curve ($\alpha = 1.0$) has an infinity at $\omega t = \pi$; its minimum value of half the steady-state current is reached a half cycle away from the peak. For $\alpha < 1$, the current does not become infinite at the bunch, nor does it fall to $\frac{1}{2} i_o$ a half cycle away from it. For $\alpha > 1$, two infinities appear, spaced symmetrically on either side of the $\alpha = 1$ peak, and the current decreases below $\frac{1}{2} i_o$ at $\omega t = 0$ and 2π.

Since the high-energy deflectors limit the target pulse to a duration δt each cycle, it is most reasonable to define the bunching factor as the ratio of the average target current with bunching to the average current without bunching over the time interval δt. Table IV gives expressions for the phase of the current maxima, the behavior of the current near the maxima, and the bunching factor B for small δt. t_o is the time at which a bunch occurs. For $\alpha \leq 1$, the time interval δt is centered around the peak at t_o. For $\alpha > 1$, t must lie in the region between the two singularities (see Figure 8), and δt extends from t_o inward.

The general features of the foregoing analysis have been observed in the operation of the proton-deuteron buncher. For a bunching distance $\ell + x$ of about 8 feet between the center of the buncher and the accelerator tube entrance, the r. f. peak voltage should be in the neighborhood of $V_o = 1$ kv for $\alpha = 1$. The predicted bunching factor for $\delta t = 3$ ns is 18. The observed factor is about 10.

The discrepancy between predicted and observed values is probably caused by energy spread in the ion source, which can amount to several hundred ev (Lefevre et al., 1962). Increasing the buncher voltage above the amount necessary for $\alpha = 1$ decreases the bunching factor. The predicted double peak can be seen by observing the target current as the relative phase of the buncher and high-energy deflector voltages is changed. In the same way, the expected decrease of a factor of 2 in the instantaneous current a half cycle from the bunch has been observed. The only optical device between the buncher and the acceleration tube is an einzel lens, which must focus the beam on the 1/4-inch stripping-canal aperture at the center of the tandem accelerator. Under normal operating conditions, very little interaction between the einzel lens and the beam energy modulation introduced by the buncher can be noticed. At $\alpha = 1$, the energy modulation in the portions of the beam near the bunch is small and is centered around zero. At larger values of α, the modulation is larger, and a shift in average beam energy will even occur near the peaks. For unusually high buncher voltages (at $\alpha = 1.5$, for example), a rapid decrease in bunching factor is observed, and the einzel lens voltage must be increased to compensate for the shift in average energy.

The bunching distance for helium extends from the helium buncher to the center of the tandem accelerator, since the neutralized atoms drift through the first acceleration tube. With $\ell + x$ approximately 38 feet, V_o must be about 5 kv for $\alpha = 1$. The observed bunching factor is 3 to 5. Interaction between the buncher and the quadrupole focussing magnet adjacent to it is pronounced. It is found that the quadrupole magnet must be operated at very low current if the buncher is to be effective at all. The poor energy stability of the helium injector provides another complication. For a continuous beam, the tandem regulation compensates adequately for small fluctuations in injector energy, but when the beam is chopped and bunched, a small change in the helium injector energy will change the phase relationship between the bunching and the chopping. It is necessary at all times to stabilize the injector energy by hand to maintain maximum average current.

REFERENCES

Ajzenberg-Selove, F., and Lauritsen, T., 1963, American Institute of Physics Handbook, 2nd ed., McGraw-Hill, New York, p. 8-71.

Ajzenberg-Selove, F., and Lauritsen, T., 1965, Nuc. Phys., to be published.

Ajzenberg-Selove, Zafiratos, and Dietrich, 1963, private communication.

Bevington, Rolland, and Lewis, 1961, Phys. Rev. 121, 871.

Blatt and Weisskopf, 1952, Theoretical Nuclear Physics, Wiley, New York, p. 360.

Cocke, C. L., 1964, private communication.

Cranberg, L., and Rosen, L., 1960, Nuclear Spectroscopy, Part A, F. Ajzenberg-Selove, ed., Academic Press, New York, p. 358.

Dietrich, Honsaker, and Davies, 1963, Bull. Am. Phys. Soc. 8, 120.

Duggan, J. L., 1962, Ph. D. Thesis, Louisiana State University (unpublished); also see Duggan, Miller, and Gabbard, Nuc. Phys. 46, 336 (1963).

Edge, R., and Peterson, G., 1962, Phys. Rev. 128, 2750.

Everling, König, Mattauch, and Wapstra, 1960, Nuc. Phys. 15, 342.

Fisher, T., and Whaling, W., 1963, Bull. Am. Phys. Soc. 8, 598.

Fisher, T., and Whaling, W., 1963a, private communication.

Fisher, T., and Whaling, W., 1964, Phys. Rev. 133, B1502.

Gabbard, Davis, and Bonner, 1959, Phys. Rev. 114, 201.

Griffiths, G. M., 1964, Nuc. Phys., to be published; also see Bull. Am. Phys. Soc. 8, 597 (1963).

Jarmie, Silbert, and Smith, 1961, Nuc. Phys. 25, 443.

Kavanagh, R. W., 1963, private communication.

Kurath, D., 1956, Phys. Rev. 101, 216.

Lefevre, H. W., and Russell, J. T., 1958, I.R.E. Proc. NS5, 146.

Lefevre, Borchers, and Poppe, 1962, Rev. Sci. Instr. 33, 1231.

Lynch, Griffiths, and Lauritsen, 1964, Nuc. Phys., to be published; also see Bull. Am. Phys. Soc, 8, 597 (1963).

McCray, J. A., 1962, Ph. D. Thesis, California Institute of Technology (unpublished).

McNally, J., 1963, private communication.

Middleton, R., and Pullen, D. J., 1964, Nuc. Phys. 51, 50.

Neiler and Good, 1960, Fast Neutron Physics, Part 1, Marion and Fowler, ed., Interscience, New York, p. 509.

Pearson, J. D., 1963, Ph. D. Thesis, California Institute of Technology (unpublished).

Sharp, Gove, and Paul, 1955, Graphs of Coulomb Functions, Atomic Energy of Canada Limited, Report No. 268.

Weber, Johnstone, and Cranberg, 1956, Rev. Sci. Instr. 27, 166.

Whaling, W., 1958, Handbuch der Physik, Vol. 34, Springer-Verlag, Berlin, p. 193.

Zafiratos, C. D., 1963, private communication.

Table I. Identification of neutron groups as corresponding to B^9 states, by observing the change in neutron energy with change in angle. The spectra of Figures 13-16 were taken at 8.7-Mev incident energy, and the spectra of Figures 17 and 18 at 11.0 Mev. See p. 20.

TABLE I. IDENTIFICATION OF B^9 STATES

E_x (Mev)	θ (lab)	Figure	χ_n	E_n (Mev)	M_{res} (amu)	$\frac{\Delta M_{res}}{\Delta \chi_n}$
12.06	0°	13, 14	60.5	4.64	9.5	5.8
	40°	15, 16	59	4.05		
14.0	0°	13, 14	49	2.71	10.2	2.0
	40°	15, 16	47	2.26		
14.67	0°	13, 14	37.5	1.77	9.2	0.8
	40°	15, 16	32.5	1.32		
16.02	0°	17	43	2.39	8.8	0.9
	30°	18	39	2.02		

Table II. Sample data calculations for the spectrum of Figure 23, using the simple analysis described in Section 2, Appendix A. See pp. 52, 57.

TABLE II. SAMPLE DATA ANALYSIS COMPUTATIONS

χ	E_n (Mev)	$\delta E_n/E_n$ * (%)	$\delta E_n/\delta\chi$ (kev/ch)	Q (Mev)	E_x (Mev)	$y_o(\chi)$ (counts/ ch)	$y(E_n)$ (counts/ 100 kev)	$Y(E_n)$ (counts/ 100 kev)
20	.956	6.2	23.3	-5.330	14.677	2520	6830	18900
44	1.938	8.8	68.4	-4.690	14.037	3199	3361	8176
61	3.956	12.6	200.	-3.102	12.449	7621	3369	9771
82	17.89	26.8	1920.	9.943	-0.596	1143	12.6	90

* (for a time resolution of 2.5 channels)

Table III. Sample data calculations for the spectrum of Figure 23, using the computer analysis described in Section 4, Appendix A. The time scale was generated from the random time spectrum of Figure 26, and was calibrated by the spectrum of Figure 25. See pp. 56, 57.

TABLE III. SAMPLE DATA ANALYSIS COMPUTATIONS

χ	τ_n (ns)	E_n (Mev)	Q (Mev)	$Y(E_n)$ (counts/ .1 Mev)	$\frac{\delta Q}{\delta E(p)}$	$\frac{\delta Q}{\delta E(He^3)}$	$\frac{\delta Q}{\delta d}$ (kev/cm)	$\frac{\delta Q}{\delta \chi_\gamma}$ (kev/ch)
20	152.78	.956	-5.330	17128±547	.56	-.73	4.9	- 14
44	105.70	1.968	-4.671	8241±200	1.37	-.77	12.0	- 51
61	73.52	3.985	-3.078	9962±128	3.20	-.81	28.0	- 175
82	33.61	17.809	9.857	96± 12	15.70	-.95	137.5	-1984

Table IV. Summary of bunching formulae for a sinusoidal voltage. The behavior of the target current at times near the bunch is shown in column 3 for the different values of α, which is proportional to the buncher peak voltage. $\alpha = 1$ represents optimum voltage. Column 4 contains the bunching factor corresponding to each range of α. See Appendix B for discussion.

TABLE IV. SUMMARY OF BUNCHING FORMULAE FOR SINUSCIDAL VOLTAGE

(See Appendix B)

α	ωt_o	$i(t)/i_o$	B	Condition on $\lvert \omega(t-t_o) \rvert$, $\omega \delta t$
<1	π	$\frac{1}{1-\alpha}$	$\frac{1}{1-\alpha}$	$<<1$
1	π	$2(6)^{-\frac{2}{3}} \lvert \omega(t-t_o) \rvert^{\frac{2}{3}}$	$6(3)^{-\frac{2}{3}}(\omega \delta t)^{-\frac{2}{3}}$	$<<1$
>1	$\pi \pm \left\{ \cos^{-1}\frac{1}{\alpha} - \sqrt{\alpha^2 - 1} \right\}$	$2^{\frac{1}{2}}(\alpha^2 - 1)^{-\frac{1}{4}} \lvert \omega(t-t_o) \rvert^{\frac{1}{2}}$	$8^{\frac{1}{2}}(\alpha^2 - 1)^{-\frac{1}{4}}(\omega \delta t)^{-\frac{1}{2}}$	$<< \sqrt{\alpha^2 - 1}$

Figure 1. Energy level diagram of B^9. The notation is standard. See pp. 1, 47.

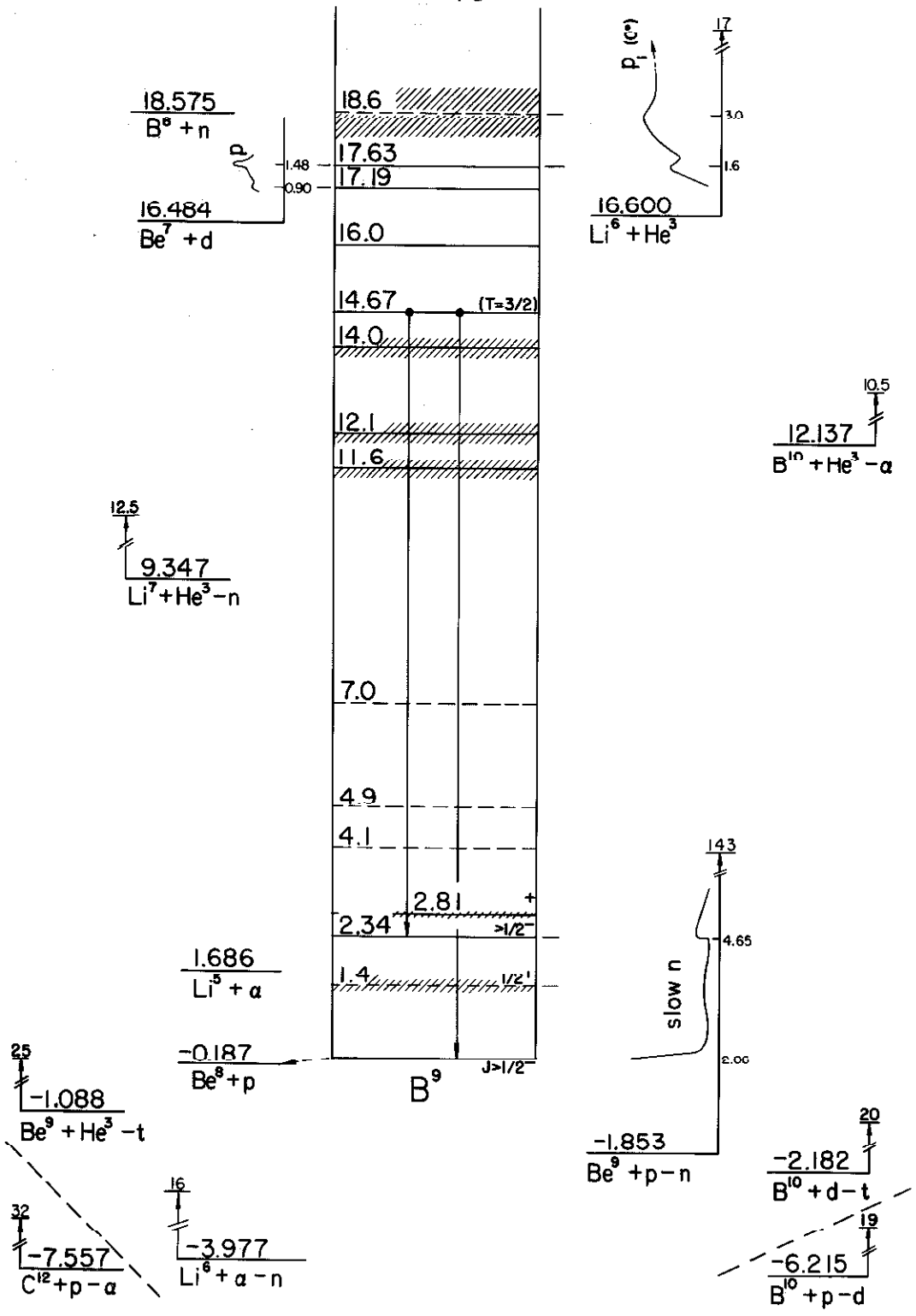
18.575
B⁸ + n
16.484
Be⁷ + d
p
1.48
0.90
18.6
17.63
17.19
16.0
14.67
(T=3/2)
14.0
12.1
11.6
7.0
4.9
4.1
2.81
+
2.34
>1/2⁻
1.4
1/2⁺
J>1/2⁻
B⁹
p₁ (c.)
17
3.0
1.6
16.600
Li⁶ + He³
10.5
12.137
B¹⁰ + He³ − α
12.5
9.347
Li⁷ + He³ − n
1.686
Li⁵ + α
−0.187
Be⁸ + p
14.3
slow n
4.65
≤.06
−1.853
Be⁹ + p − n
25
−1.088
Be⁹ + He³ − t
20
−2.182
B¹⁰ + d − t
19
−6.215
B¹⁰ + p − d
16
−3.977
Li⁶ + α − n
32
−7.557
C¹² + p − α

Figure 1

Figure 2. Level diagrams of the mass-nine nuclei, including the results of recent experimental investigations. The notation is that of Ajzenberg-Selove and Lauritsen (1963). The ground-state energies of Li^9 and B^9 have been adjusted by removing the coulomb-energy difference and the neutron-proton mass difference of the pairs Li^9-Be^9 and Be^9-B^9. See pp. 2, 42.

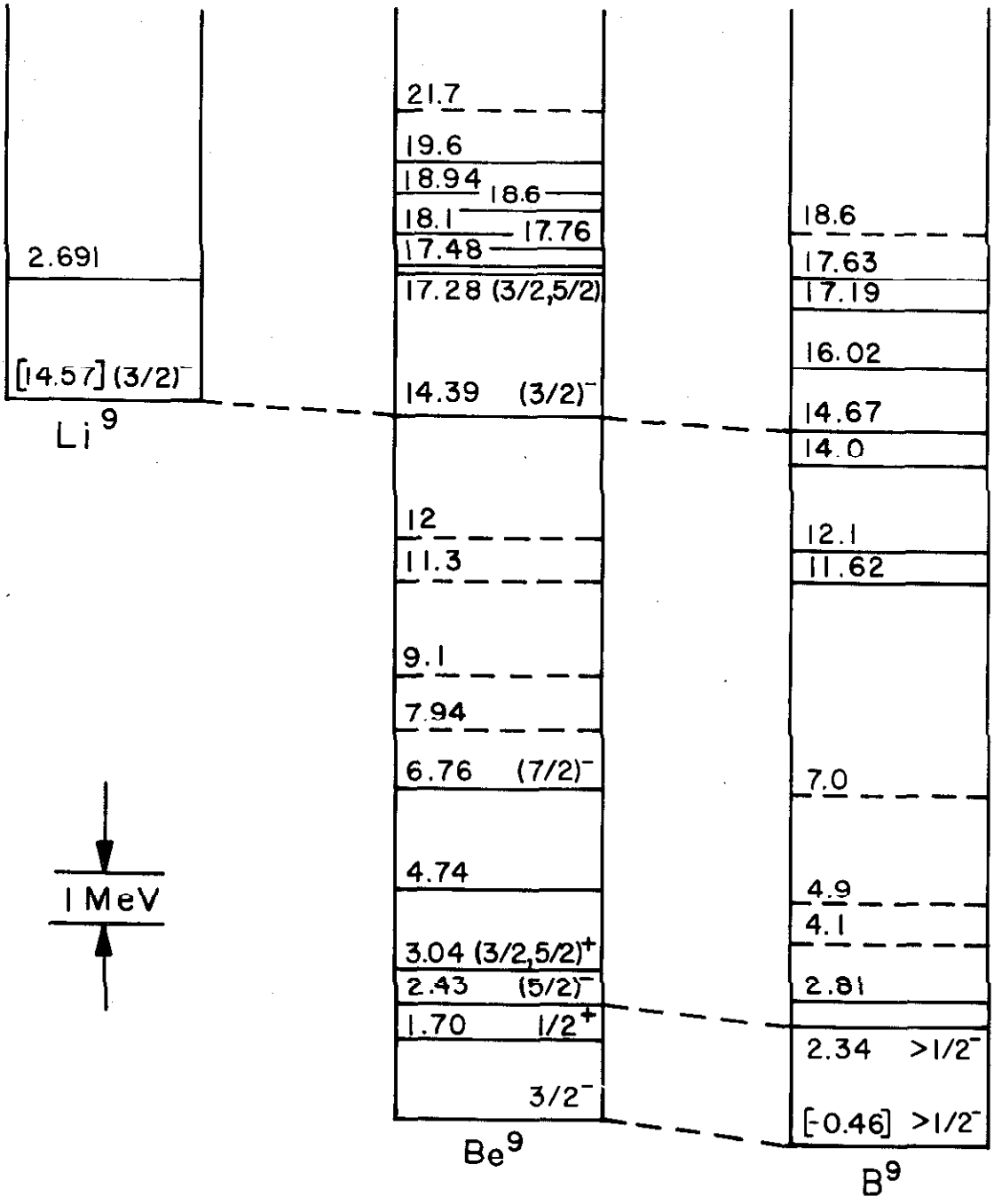
2.691
[14.57] (3/2)⁻
Li⁹
21.7
19.6
18.94
18.6
18.1
17.76
17.48
17.28 (3/2,5/2)
14.39 (3/2)⁻
12
11.3
9.1
7.94
6.76 (7/2)⁻
4.74
3.04 (3/2,5/2)⁺
2.43 (5/2)⁻
1.70 1/2⁺
3/2⁻
Be⁹
1 MeV
18.6
17.63
17.19
16.02
14.67
14.0
12.1
11.62
7.0
4.9
4.1
2.81
2.34 >1/2⁻
[-0.46] >1/2⁻
B⁹

Figure 2

Figure 3. Mass excesses of all combinations of nucleons that can be formed by He^3 bombardment of Li^7 at energies up to 15 Mev. See pp. 3, 35.

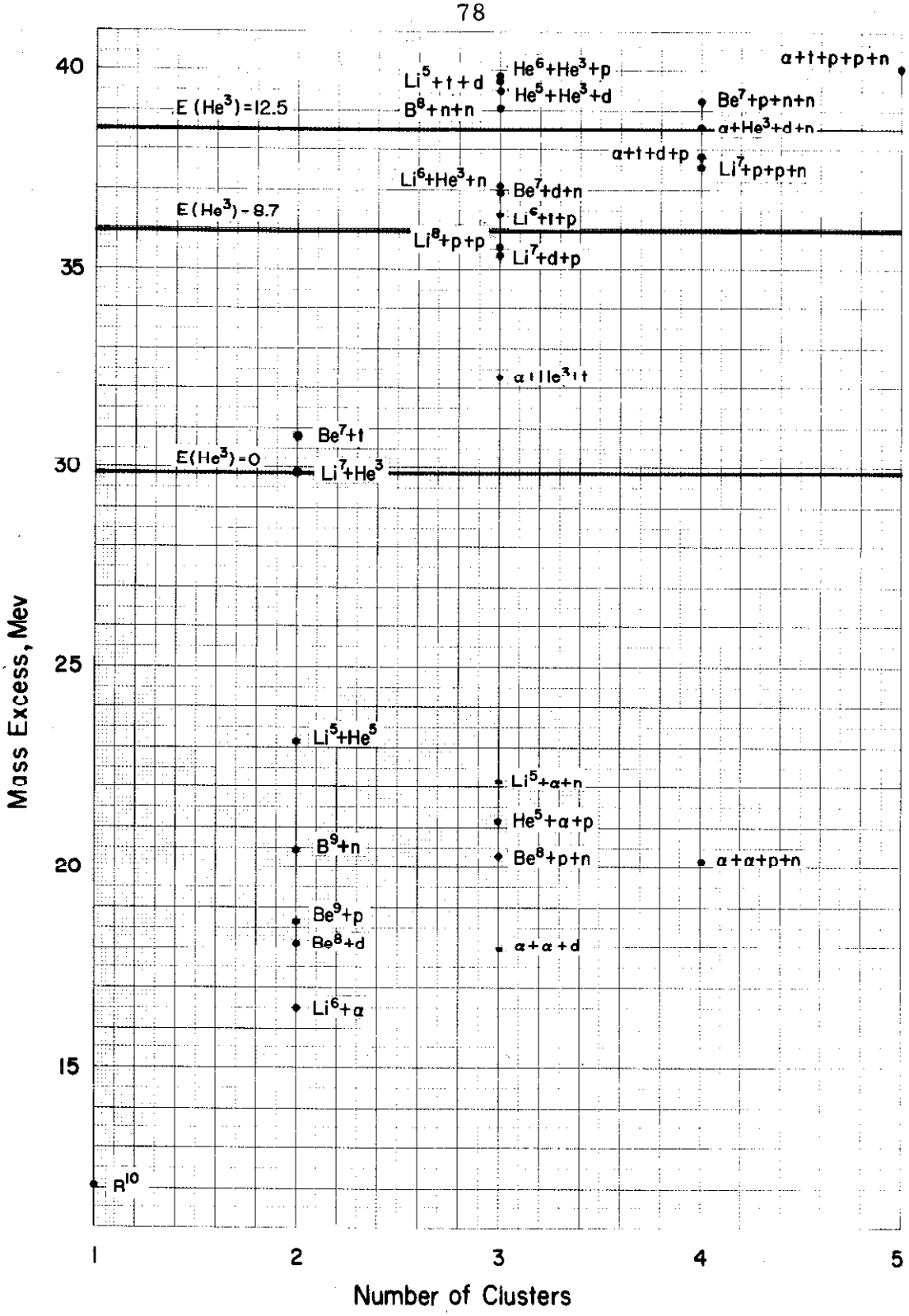
40
35
30
25
20
15
Mass Excess, Mev
1
2
3
4
5
Number of Clusters
E (He3) = 12.5
E (He3) = 8.7
E (He3) = 0
Li5 + t + d
He6 + He3 + p
He5 + He3 + d
B8 + n + n
α + t + p + p + n
Be7 + p + n + n
α + He3 + d + n
α + t + d + p
Li7 + p + p + n
Li6 + He3 + n
Be7 + d + n
Li6 + t + p
Li8 + p + p
Li7 + d + p
α + He3 + t
Be7 + t
Li7 + He3
Li5 + He5
Li5 + α + n
He5 + α + p
B9 + n
Be8 + p + n
α + α + p + n
Be9 + p
Be8 + d
α + α + d
Li6 + α
R10

Figure 3

Figure 4. Block diagram of the time-of-flight spectrometer used with the ONR-CIT tandem accelerator. See Part II.

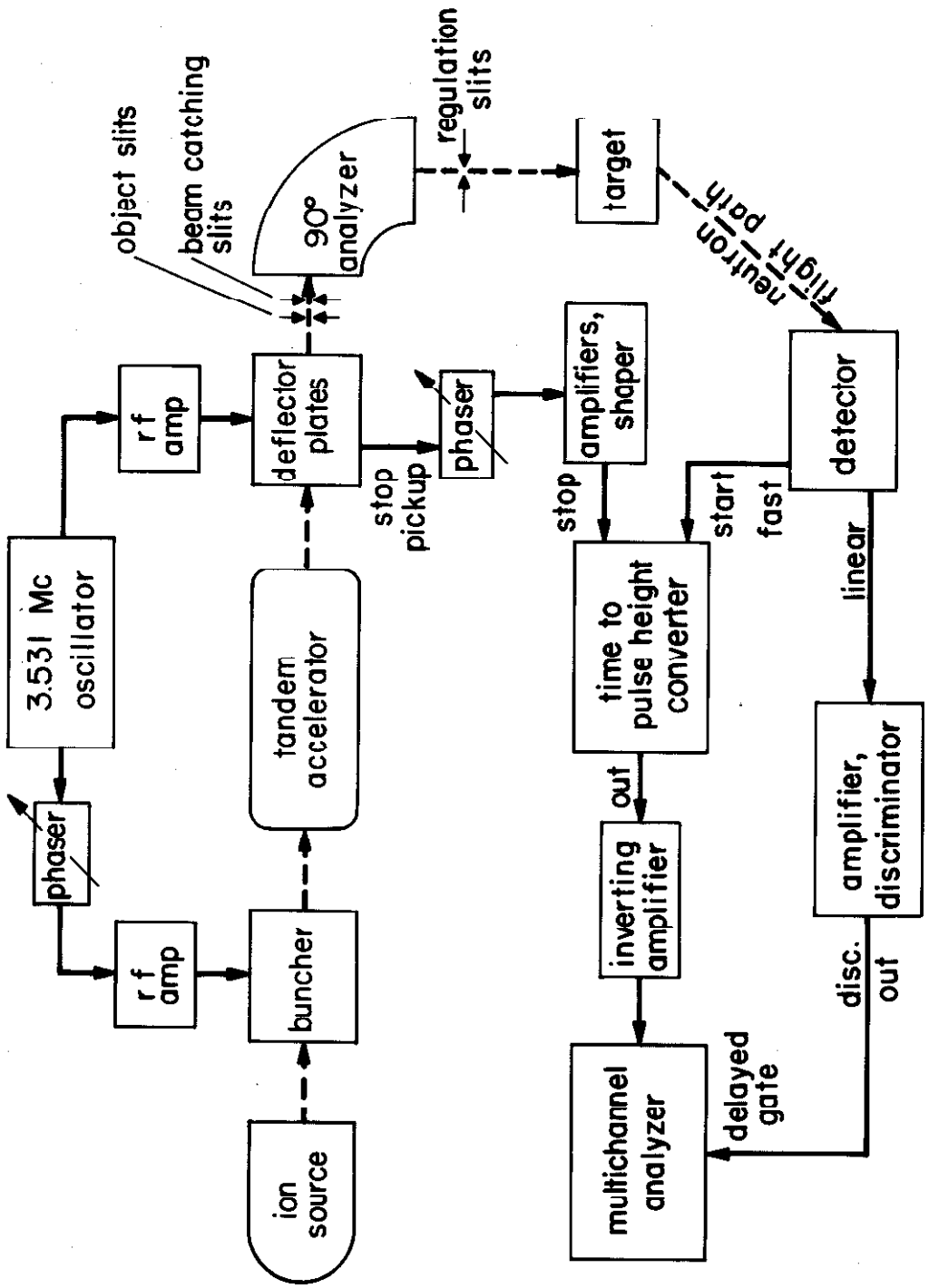
object slits
beam catching slits
90° analyzer
regulation slits
target
neutron flight path
r f amp
deflector plates
phaser
amplifiers, shaper
detector
3.531 Mc oscillator
stop pickup
stop
start
fast
phaser
tandem accelerator
time to pulse height converter
linear
r f amp
buncher
out
inverting amplifier
amplifier, discriminator
ion source
multichannel analyzer
delayed gate
disc. out

Figure 4

Figure 5. a. Illustration of the paths taken by particles traversing the deflector plates and passing through the beam-catching slit assembly, showing the division of the beam into two components. See p. 6. b. Schematic diagram of the buncher assemblies. See pp. 7, 9.

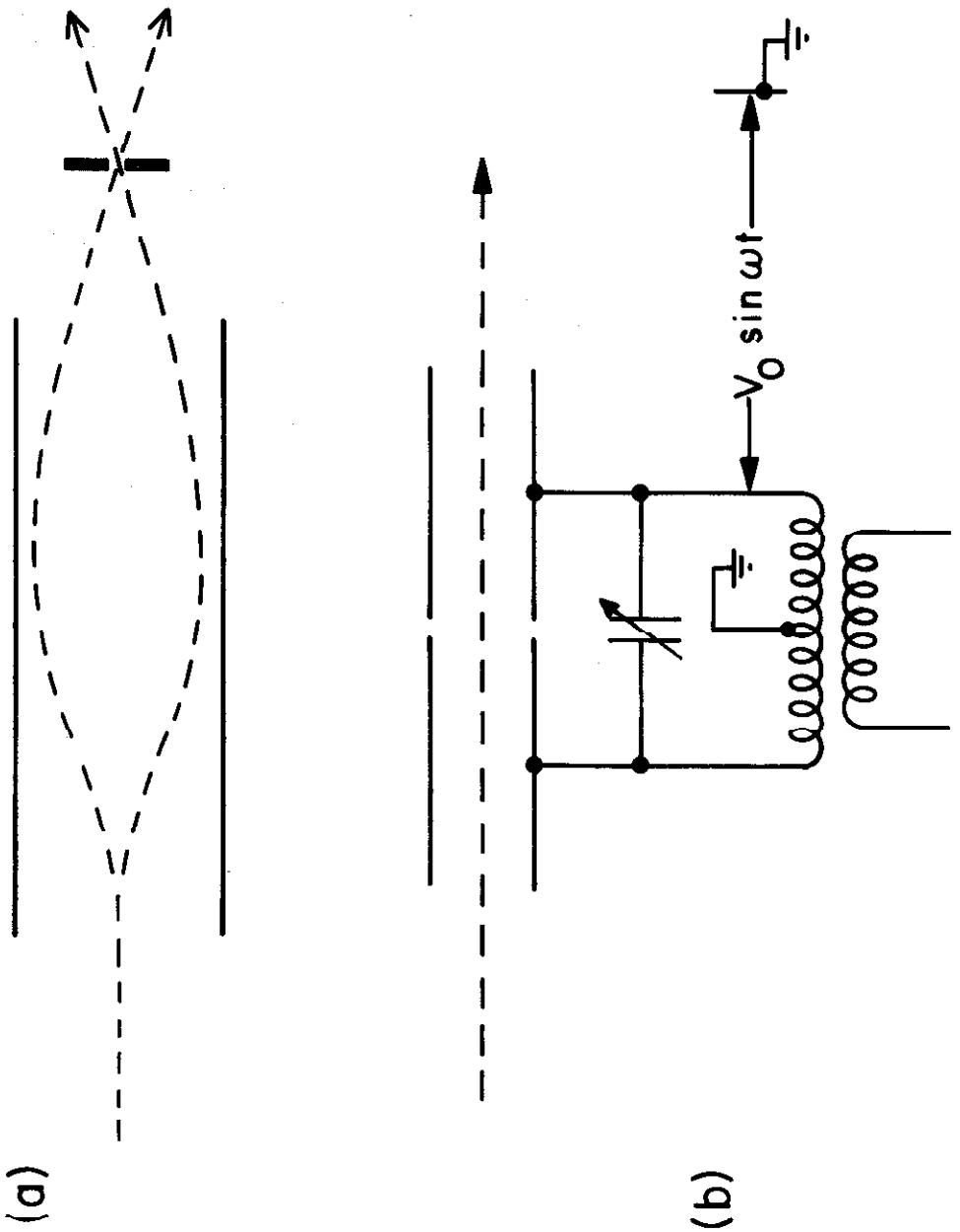

Figure 5

Figure 6. Graph of the relation (4), p. 59, between the phase $\omega t'$ at which particles enter the buncher, and the phase ωt at which they reach the target. α is proportional to the r. f. voltage applied to the buncher.

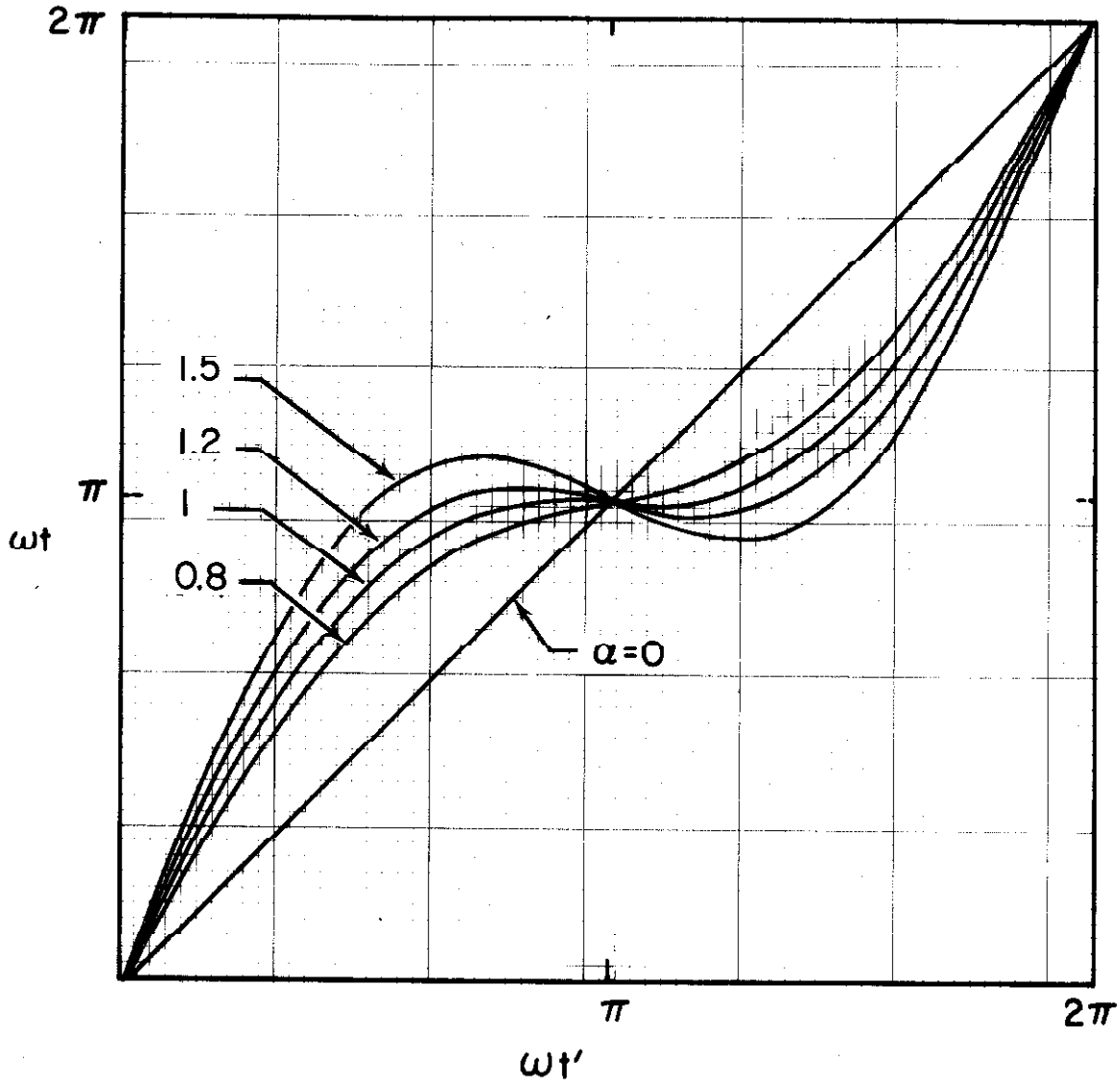

Figure 6

Figure 7. Graphs of the instantaneous target current predicted by expression (5), p. 59. α is proportional to the r. f. voltage applied to the buncher. $\alpha = 0$ represents the unbunched beam; $\alpha = 1.0$, optimum bunching voltage; and $\alpha = 0.8$, slightly less than the optimum value.

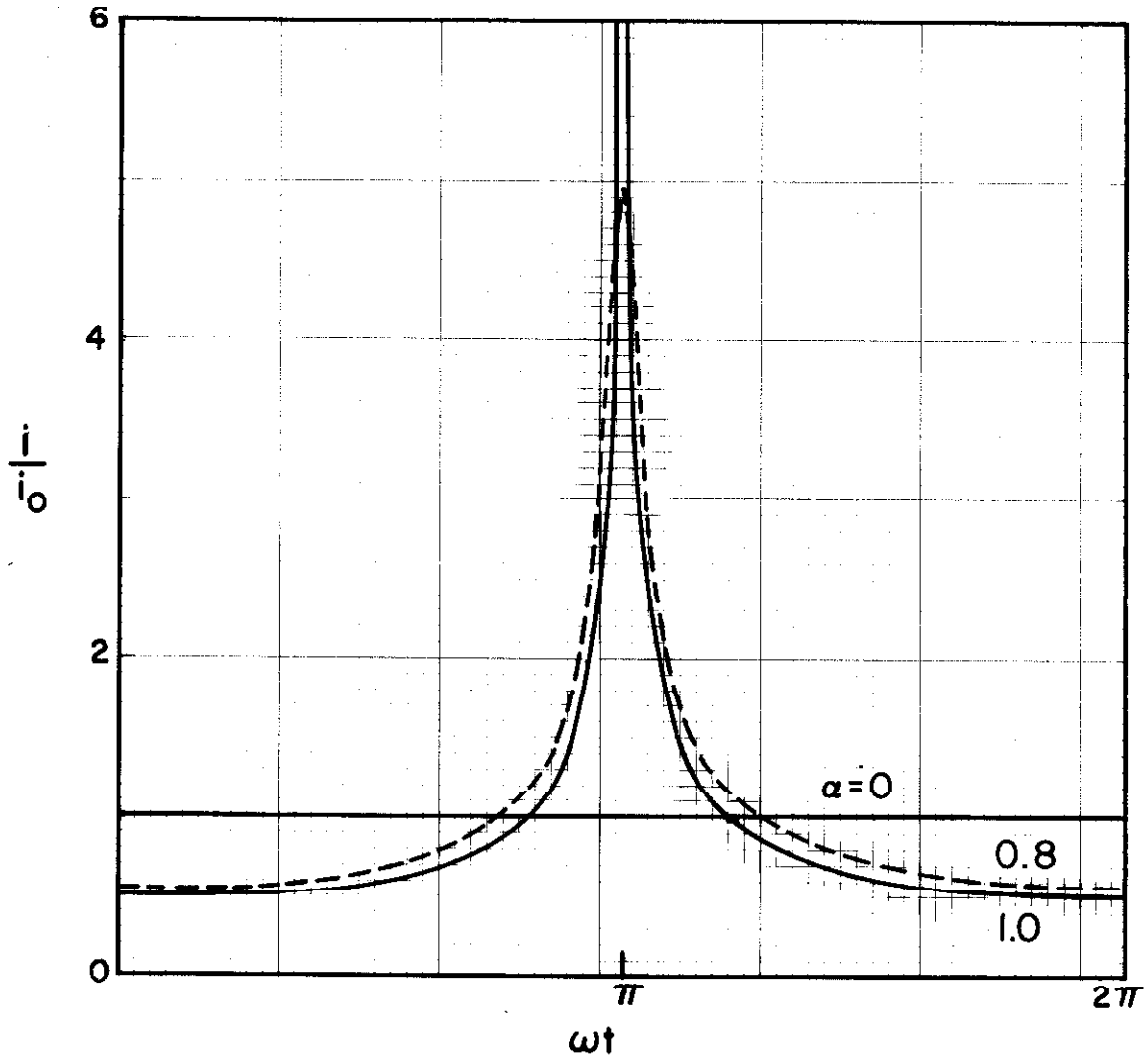

Figure 7

Figure 8. Graphs of the instantaneous target current predicted by expression (5), p. 59. α is proportional to the r. f. voltage applied to the buncher. $\alpha = 0$ represents the unbunched beam; $\alpha = 1.0$, optimum bunching voltage; and $\alpha = 1.5$, excess voltage.

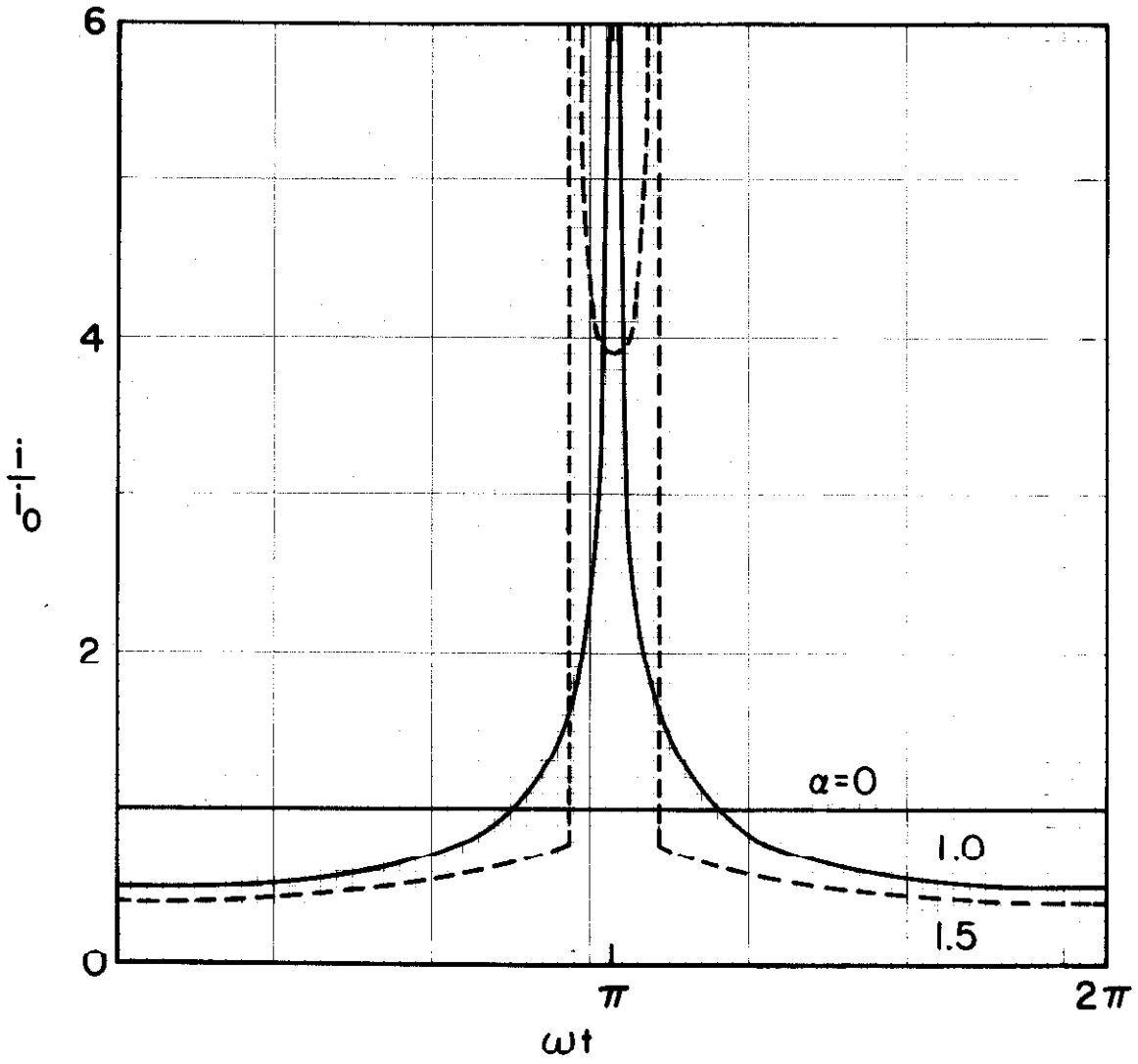

Figure 8

Figure 9. Time spectrum of neutrons from the $Li^7(p,n)Be^7$ reaction, at an incident energy of 3.434 Mev, flight path 1.85 m, and angle 0°. The gamma peak is near $\chi = 85$; the peaks near $\chi = 34$ and $\chi = 25$ are neutrons corresponding to the ground and first excited Be^7 states, respectively. The open circles mark every tenth channel. See pp. 13, 27, 34.

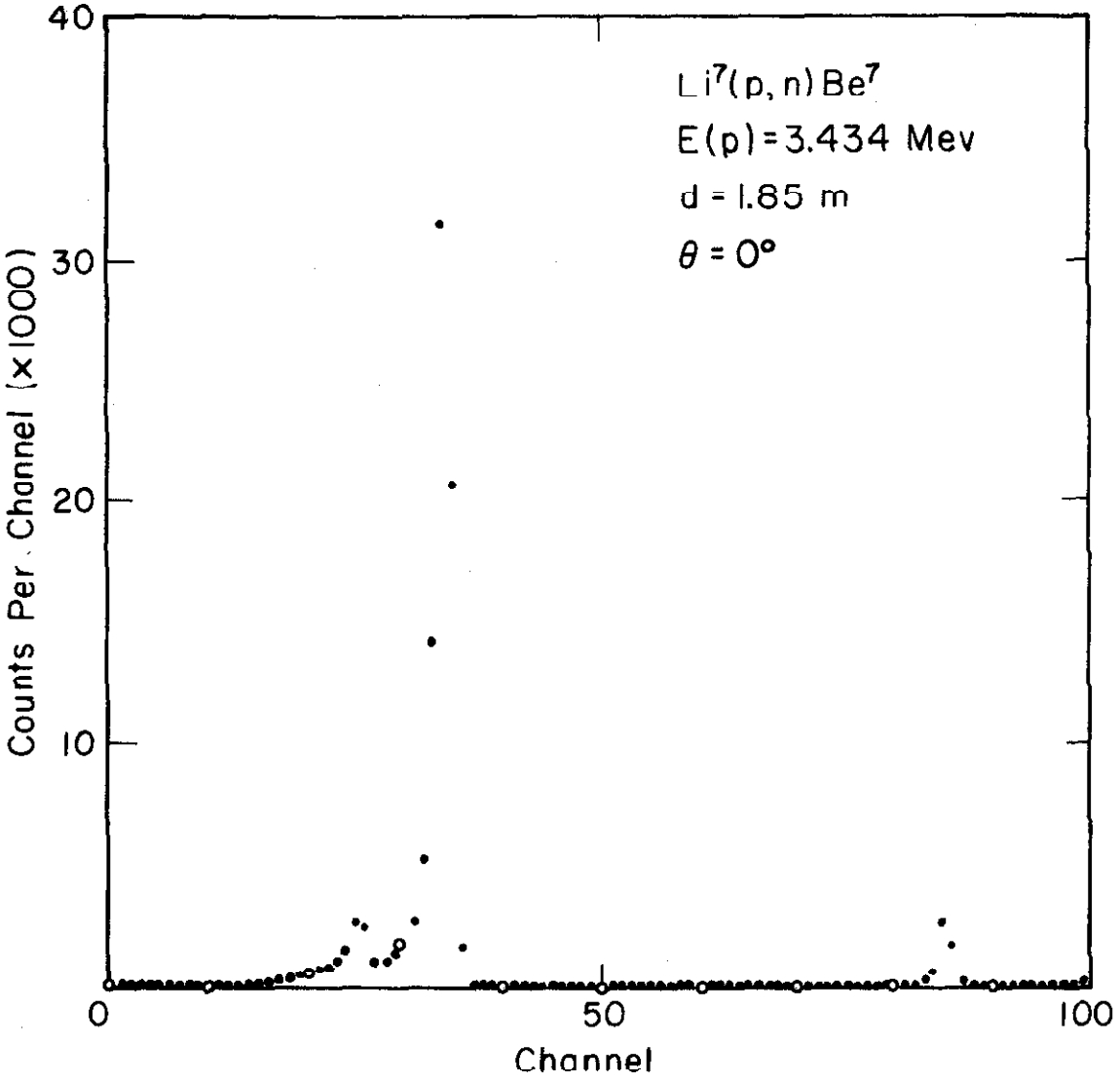
Li⁷(p, n)Be⁷
E(p) = 3.434 Mev
d = 1.85 m
θ = 0°
Counts Per Channel (x1000)
40
30
20
10
0
50
100
Channel

Figure 9

Figure 10. Time spectrum of neutrons from the $Li^7(He^3,n)B^9$ reaction, at incident energy 10.5 Mev, flight path 1.85 m, and angle 0°. The peak near $\chi = 15$ is a spurious gamma peak; the neutron groups near $\chi = 37$, 52, and 62 correspond to excited states of B^9 at $E_x = 16.02$, 14.67, and 12.06 Mev, respectively. See pp. 14, 34, 38.

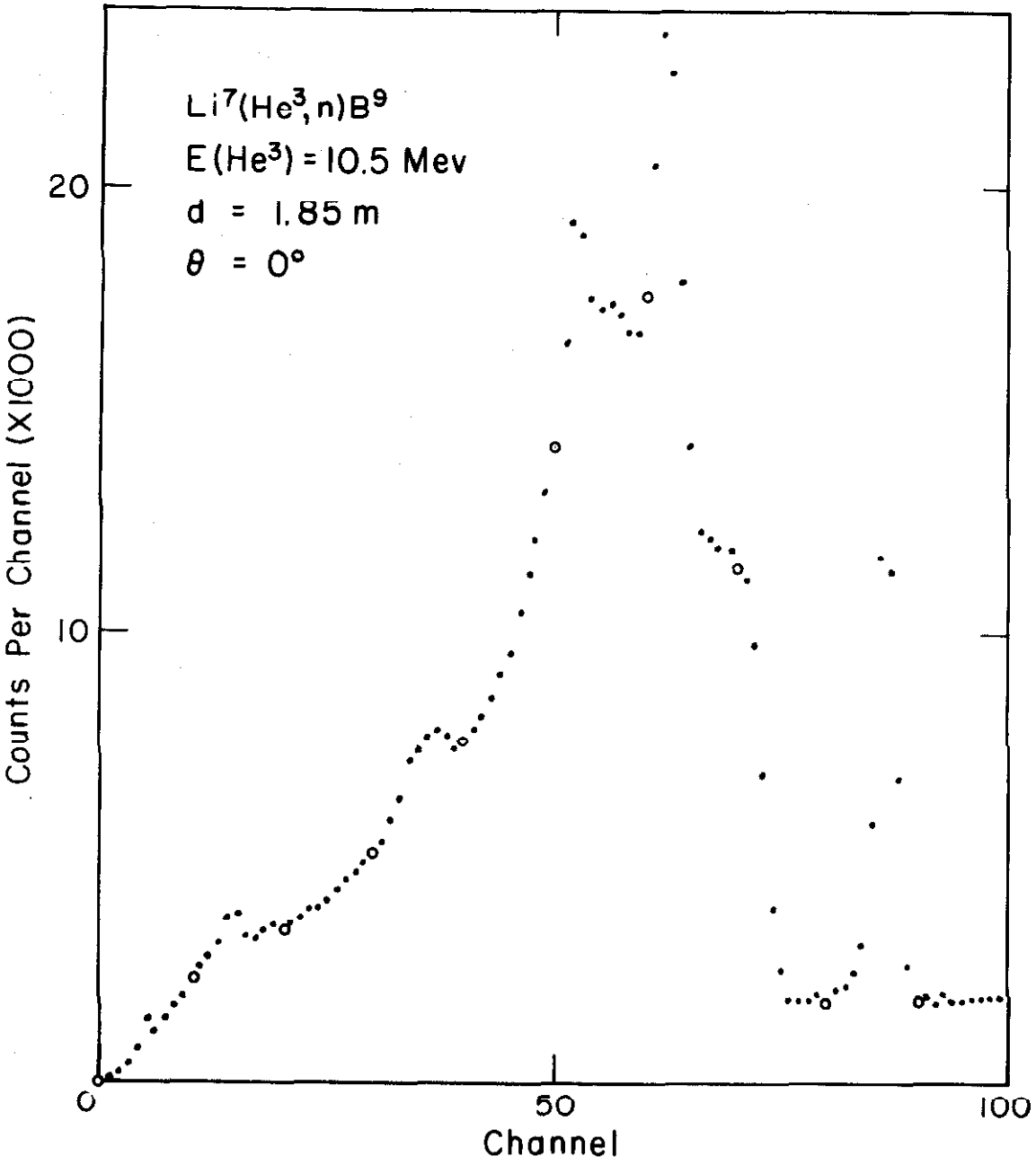
Li7(He3,n)B9
E(He3) = 10.5 Mev
d = 1.85 m
θ = 0°
Counts Per Channel (X1000)
20
10
0
50
100
Channel

Figure 10

Figure 11. Cs^{137} gamma spectrum taken from the "linear" photomultiplier output. For convenience, only every fifth point has been shown. The side-channel discriminator level is set on the right-hand slope of the Cs^{137} peak. See p. 15.

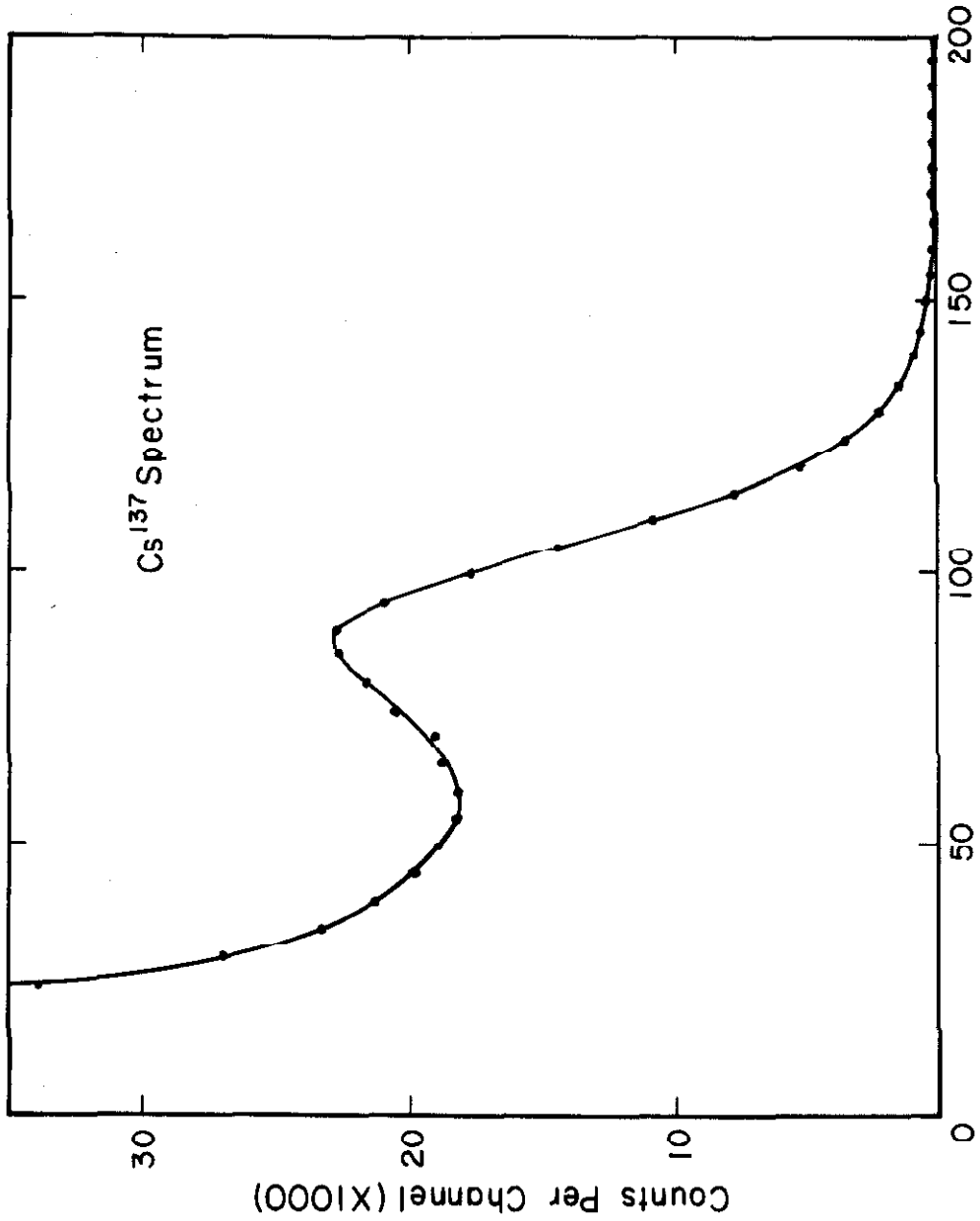
Cs137 Spectrum
Counts Per Channel (X1000)
0
10
20
30
0
50
100
150
200
Channel

Figure 11

Figure 12. Relative sensitivity of the neutron detector. The experimental points were measured by using the $Li^7(p,n)Be^7$ reaction, and the solid curve was computed from expression (1), p. 16. See p. 16.

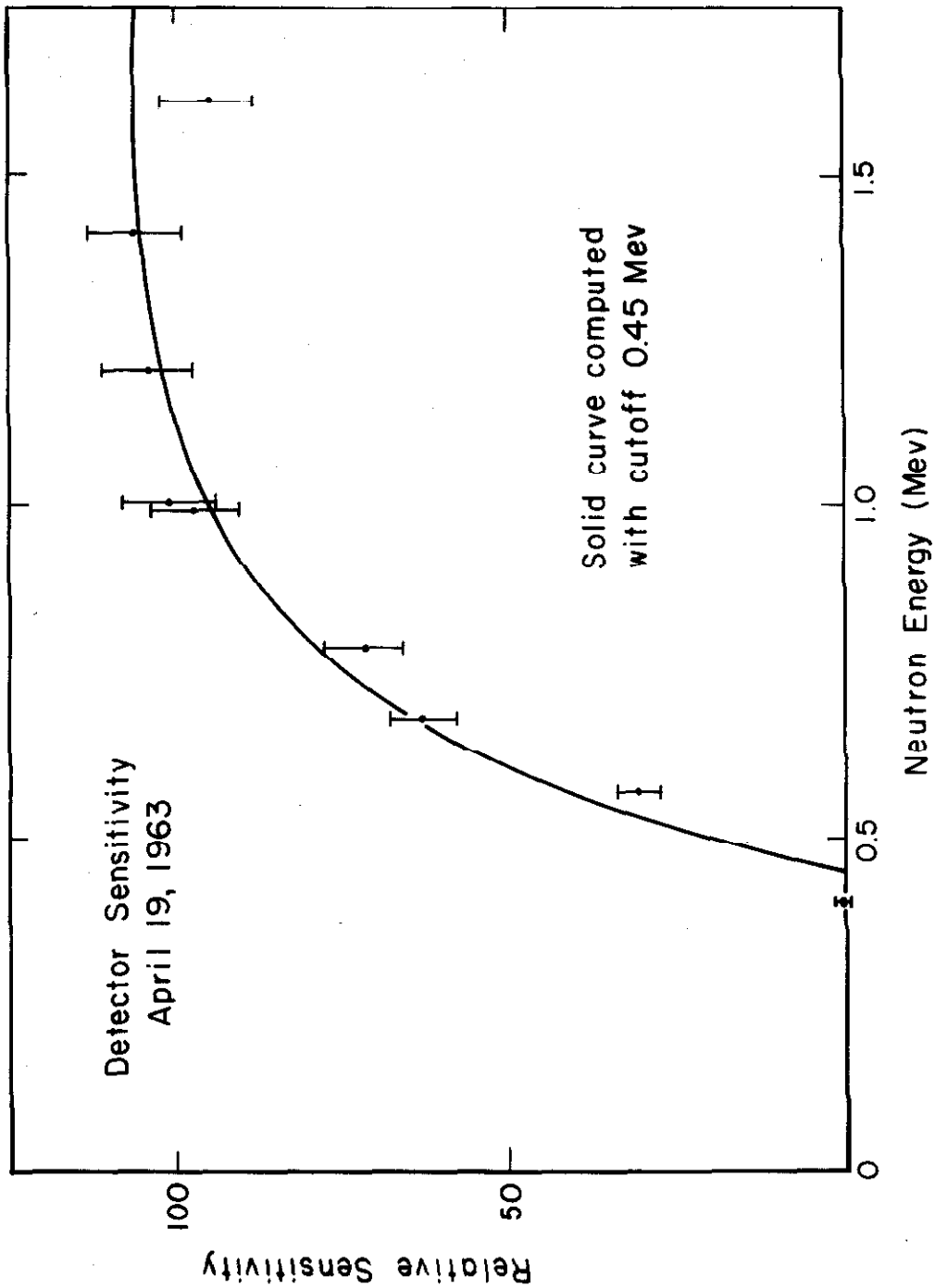
Detector Sensitivity
April 19, 1963
Solid curve computed
with cutoff 0.45 Mev
Relative Sensitivity
100
50
0
0.5
1.0
1.5
Neutron Energy (Mev)

Figure 12

Figure 13. Time spectrum showing neutron groups near $\chi = 38$ and 61, corresponding to B^9 states at $E_x = 14.67$ and 12.06 Mev, respectively. The neutron group corresponding to the 14.0-Mev state, centered around $\chi = 49$, is obscured by the shape of the continuum. A spurious gamma peak occurs near $\chi = 21$. See pp. 20, 22, 39.

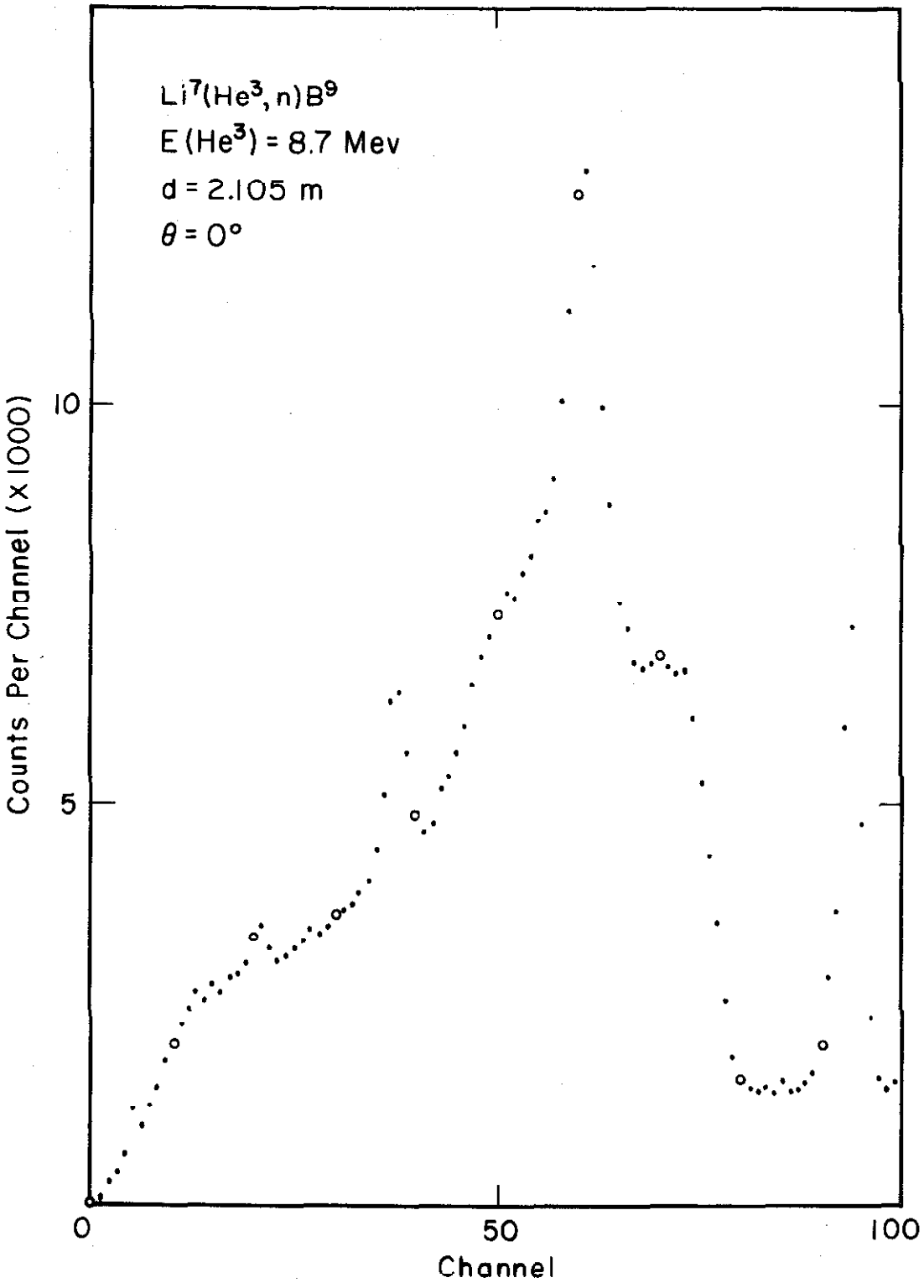
Li7(He3, n)B9
E (He3) = 8.7 Mev
d = 2.105 m
θ = 0°
Counts Per Channel (x 1000)
10
5
0
50
100
Channel

Figure 13

Figure 14. A portion of the spectrum of Figure 13 converted to a counts-vs.-energy presentation by the computer program described in Appendix A. The neutron groups corresponding to the B^9 levels at 14.67, 14.0, and 12.06 Mev appear near E_n = 1.8, 2.7, and 4.6 Mev, respectively. The dashed line indicates the continuum subtraction chosen for cross-section and angular-distribution measurements. See pp. 20, 30, 36.

Note suppressed zero.

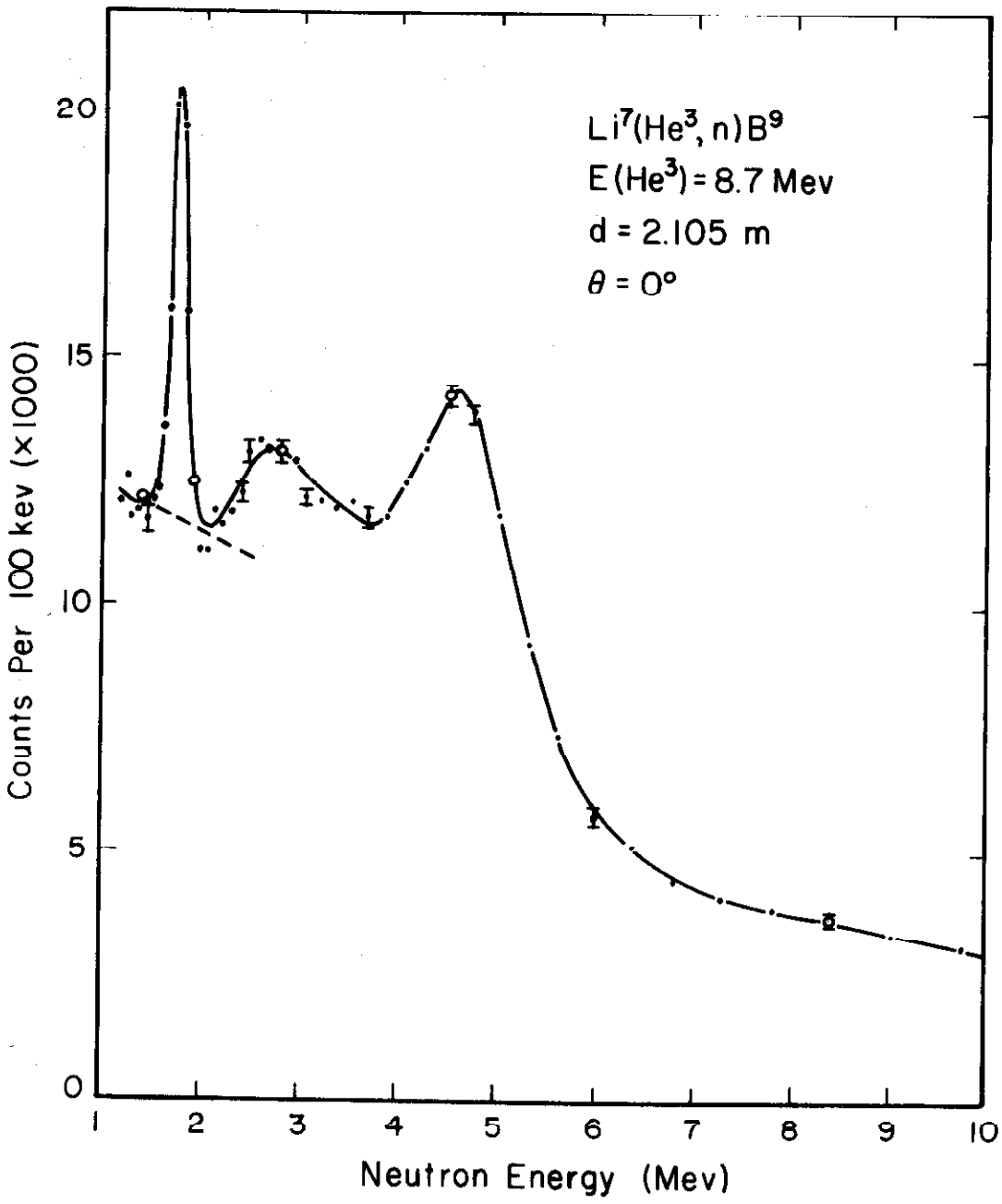
Li7(He3, n)B9
E(He3) = 8.7 Mev
d = 2.105 m
θ = 0°
Counts Per 100 kev (×1000)
Neutron Energy (Mev)
0
5
10
15
20
1
2
3
4
5
6
7
8
9
10

Figure 14

Figure 15. Time spectrum showing neutron groups near $\chi = 33$ and 60, corresponding to B^9 states at $E_x = 14.67$ and 12.06 Mev. respectively. The neutron group corresponding to the 14.0-Mev state, centered around $\chi = 47$, is obscured by the shape of the continuum. A spurious gamma peak occurs near $\chi = 18$. See pp. 20, 39.

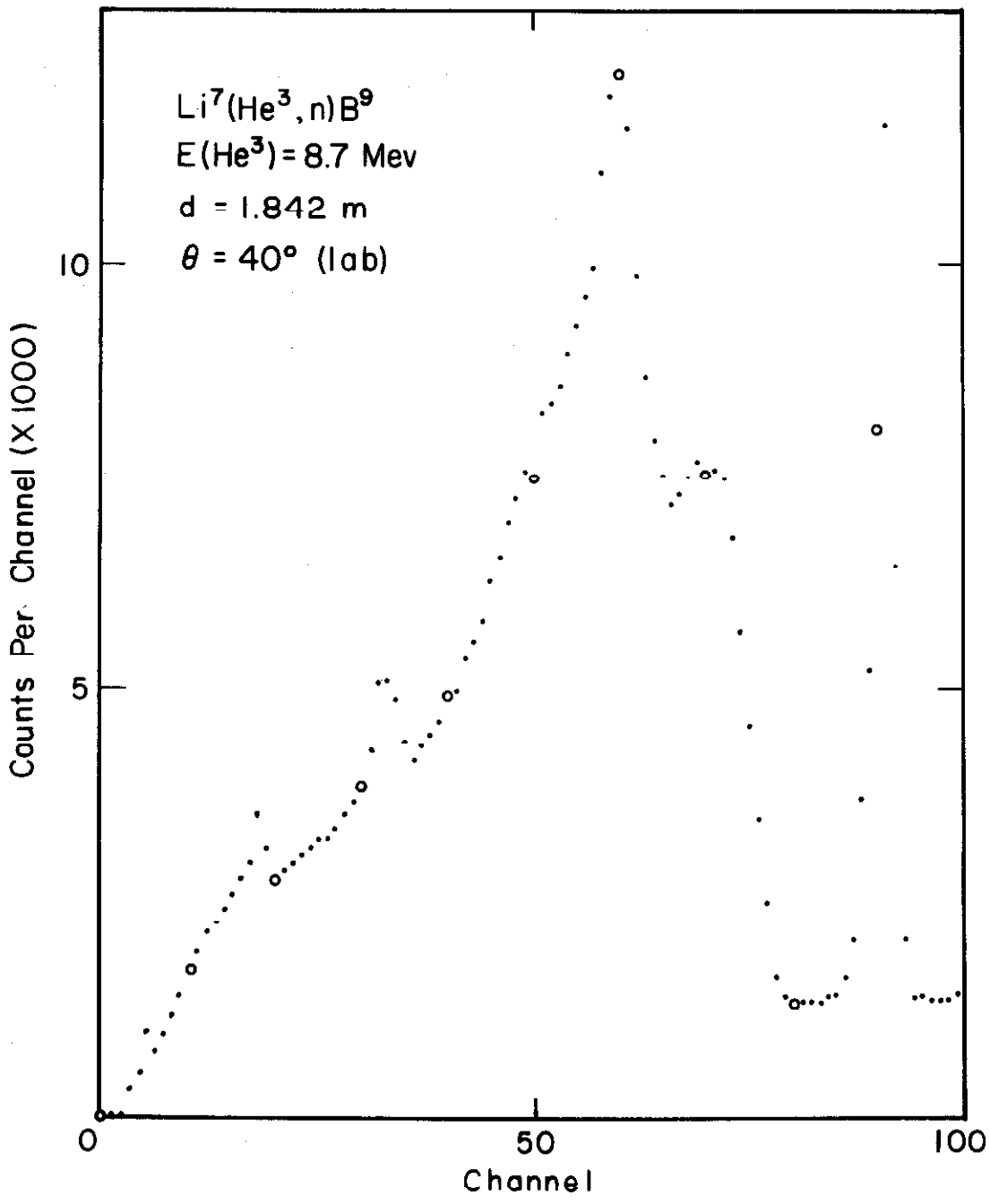
Li7(He3, n)B9
E(He3) = 8.7 Mev
d = 1.842 m
θ = 40° (lab)
Counts Per Channel (X 1000)
10
5
0
50
100
Channel

Figure 15

Figure 16. A portion of the spectrum of Figure 15 converted to a counts-vs.-energy presentation by the computer program described in Appendix A. The neutron groups corresponding to the B^9 levels at 14.67, 14.0, and 12.06 Mev appear near E_n = 1.3, 2.3, and 4.1 Mev, respectively. The dashed line indicates the continuum subtraction chosen for cross-section and angular-distribution measurements.

See p. 20.

Note suppressed zero.

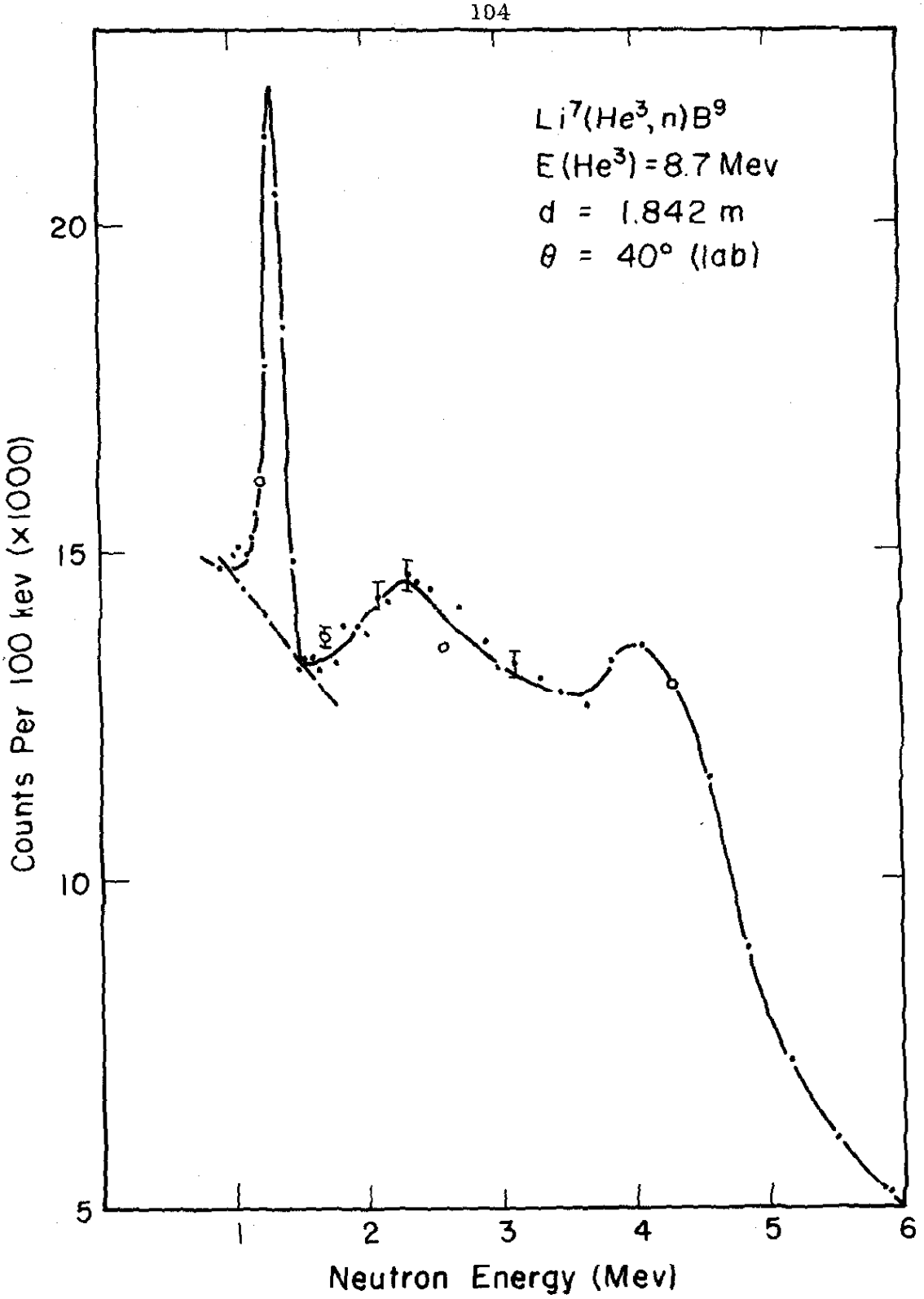
Li7(He3, n)B9
E(He3) = 8.7 Mev
d = 1.842 m
θ = 40° (lab)
Counts Per 100 kev (x1000)
20
15
10
5
1
2
3
4
5
6
Neutron Energy (Mev)

Figure 16

Figure 17. Time spectrum showing a neutron group near $\chi = 43$ corresponding to the 16.02-Mev B^9 state. The energy of the group is 2.39 Mev. The groups near $\chi = 54$ and 63 correspond to the B^9 levels at $E_x = 14.67$ and 12.06 Mev, respectively. The group near $\chi = 13$ is a spurious gamma peak. See p. 20.

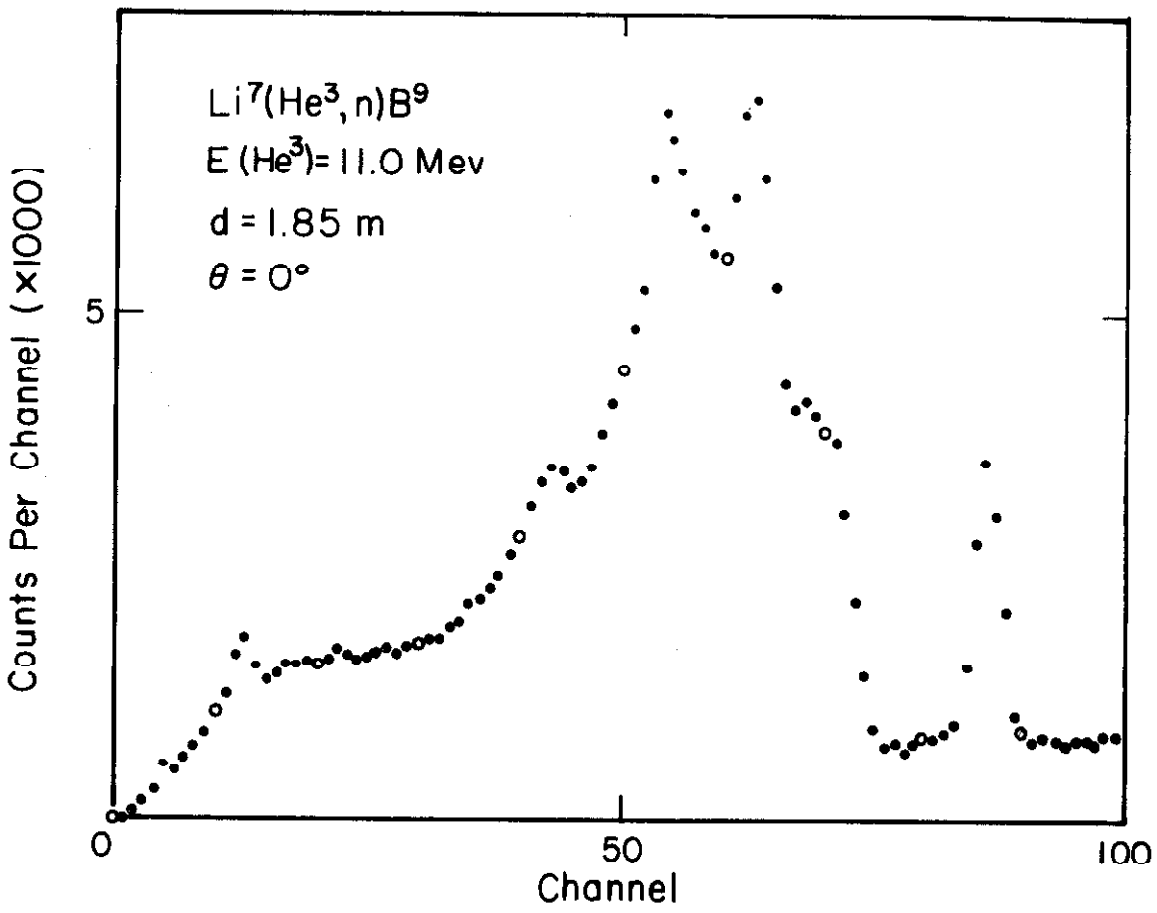
Li7(He3, n)B9
E (He3)= 11.0 Mev
d = 1.85 m
θ = 0°
Counts Per Channel (x1000)
5
0
50
100
Channel

Figure 17

Figure 18. Time spectrum showing a neutron group near $\chi = 39$ corresponding to the 16.02-Mev B^9 state. The energy of the group is 2.02 Mev. The groups near $\chi = 53$ and 62 correspond to the B^9 levels at $E_x = 14.67$ and 12.06 Mev, respectively. The group near $\chi = 13$ is a spurious gamma peak. See p. 20.

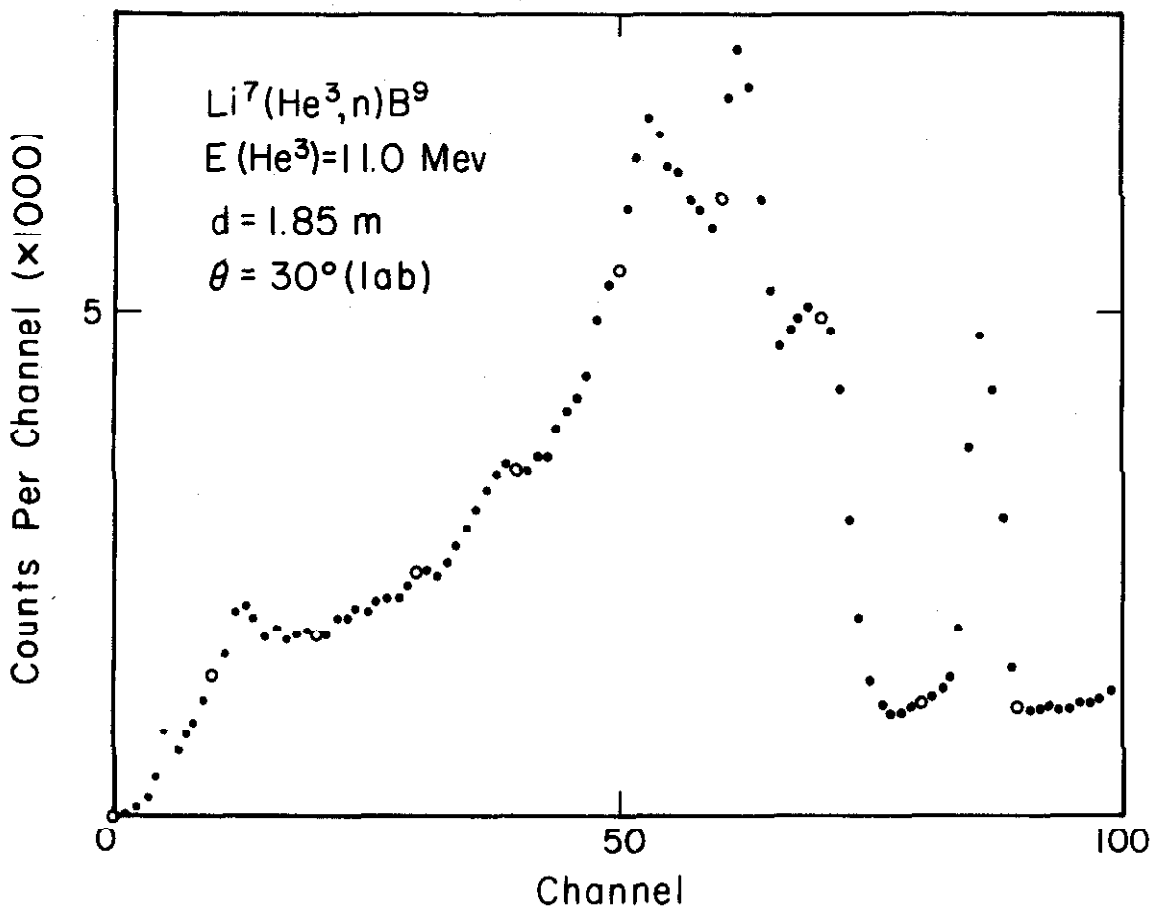
Li⁷(He³,n)B⁹
E(He³)=11.0 Mev
d = 1.85 m
θ = 30°(lab)
Counts Per Channel (x1000)
5
0
50
100
Channel

Figure 18

Figure 19. Time spectrum at 7.14-Mev incident energy. The wide structure near $\chi = 28$ corresponds to the 12.06-Mev B^9 state. See p. 21.

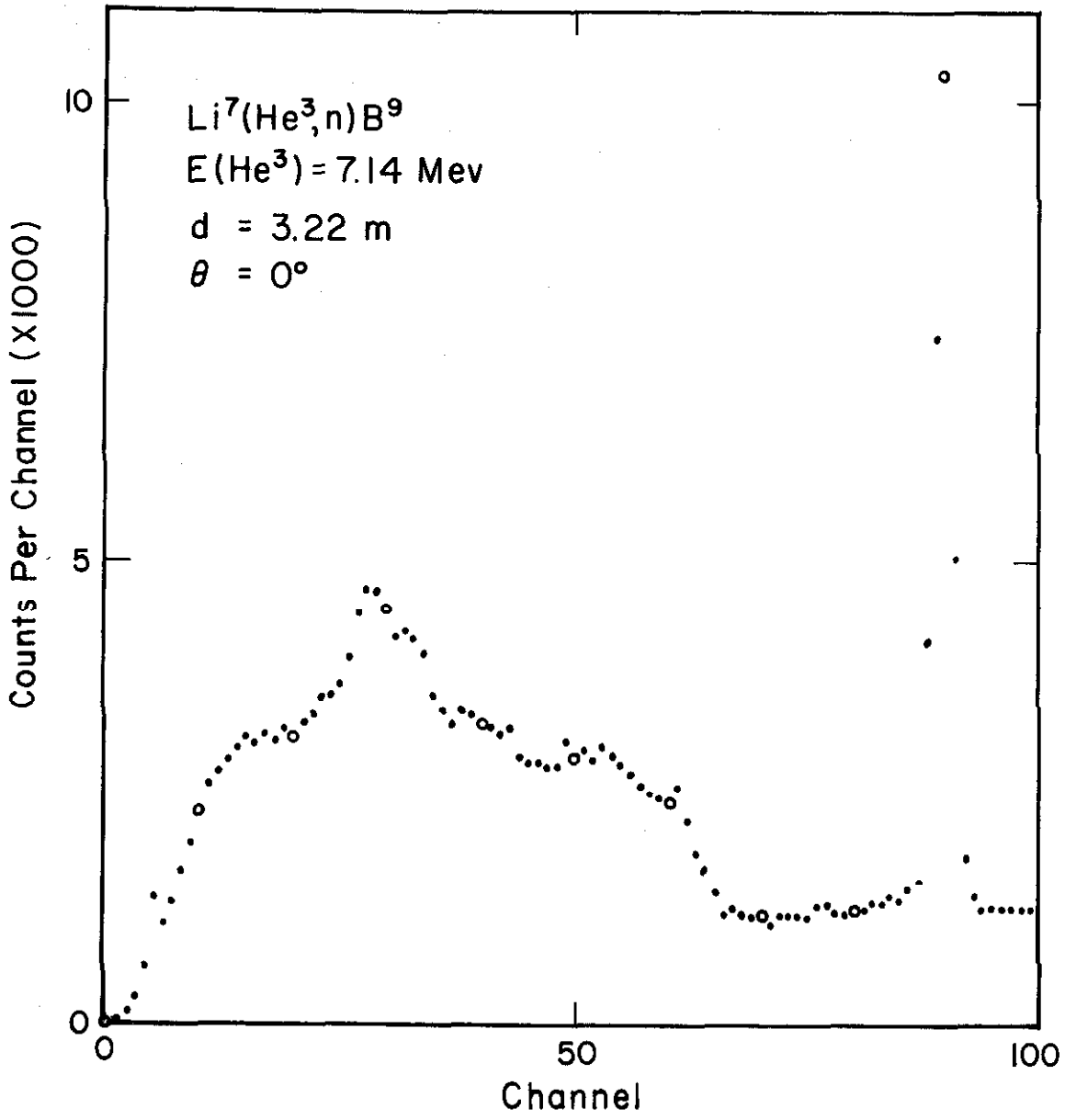
Li⁷(He³,n)B⁹
E(He³) = 7.14 Mev
d = 3.22 m
θ = 0°
Counts Per Channel (X1000)
10
5
0
0
50
100
Channel

Figure 19

Figure 20. A portion of the spectrum of Figure 19 converted to the counts-vs.-energy presentation. The peak near E_n = 3.3 Mev corresponds to the 12.06-Mev B^9 level.

See pp. 21, 30.

Note suppressed zero.

Sensitivity cutoff E_o = 0.65 Mev.

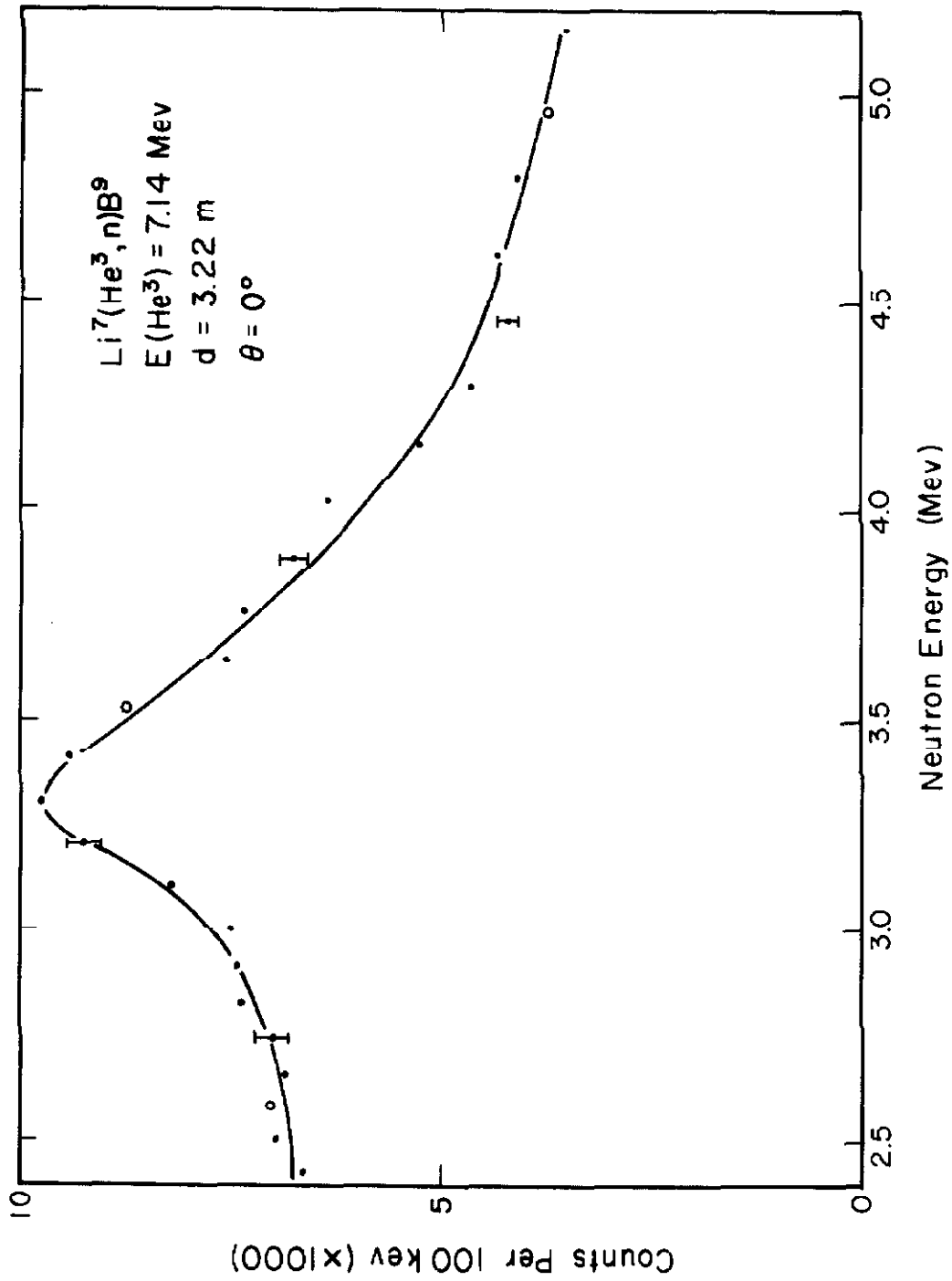
$Li^7(He^3,n)B^9$
$E(He^3) = 7.14$ Mev
d = 3.22 m
$\theta = 0°$
Counts Per 100 kev (x1000)
Neutron Energy (Mev)
10
5
0
2.5
3.0
3.5
4.0
4.5
5.0

Figure 20

Figure 21. Time spectrum at 7.14-Mev incident energy. The wide structure near $\chi = 26$ corresponds to the 12.06-Mev B^9 state. See p. 21.

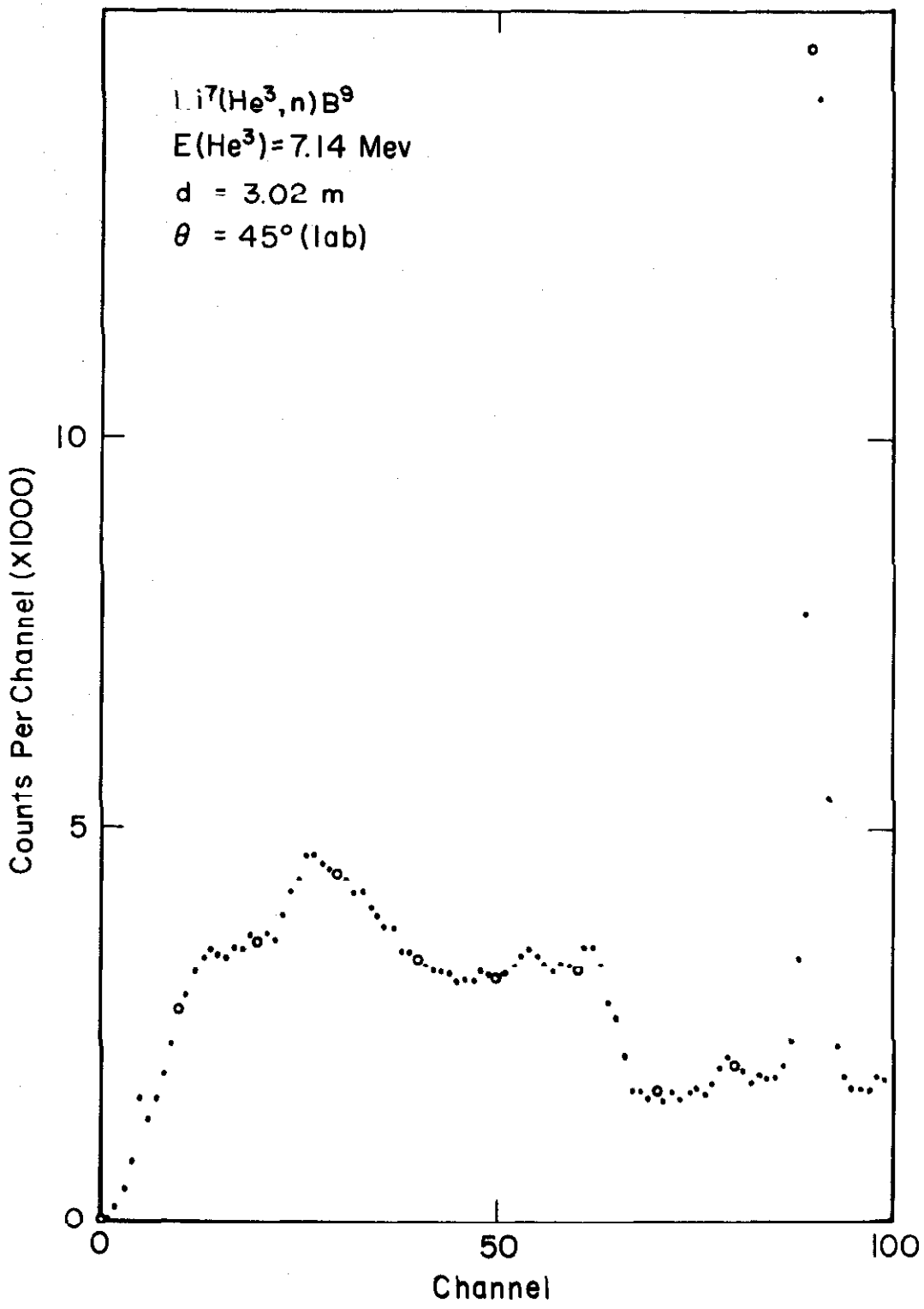
Li7(He3,n)B9
E(He3)=7.14 Mev
d = 3.02 m
θ = 45° (lab)
Counts Per Channel (X1000)
10
5
0
0
50
100
Channel

Figure 21

Figure 22. A portion of the spectrum of Figure 21 converted to the counts-vs.-energy presentation. The peak near E_n = 2.7 Mev corresponds to the 12.06-Mev B^9 level. See p. 21.

Note suppressed zero.

Sensitivity cutoff E_o = 0.65 Mev.

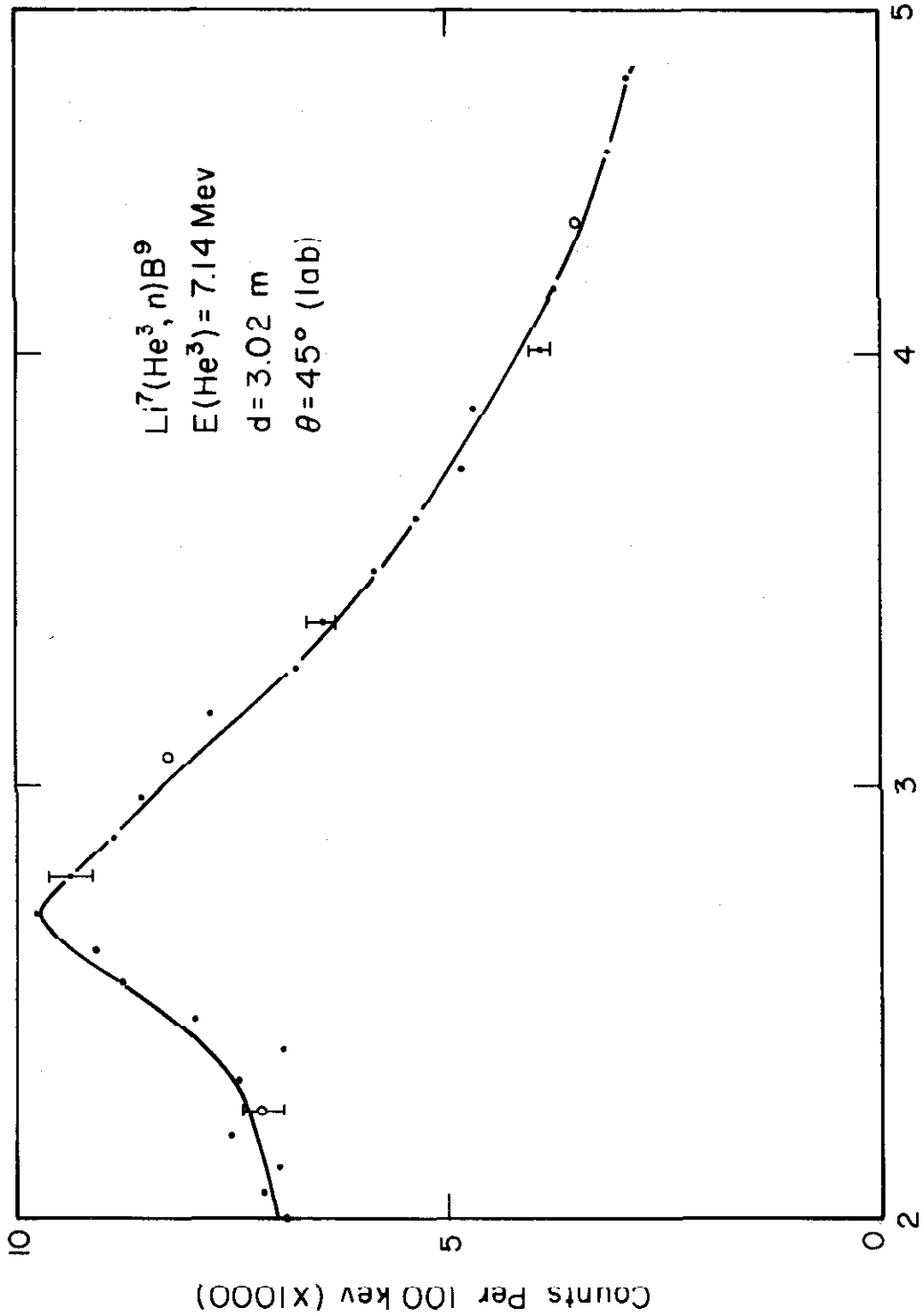
$Li^7(He^3, n)B^9$
$E(He^3) = 7.14$ Mev
d = 3.02 m
$\theta = 45°$ (lab)
Counts Per 100 kev (X1000)
Neutron Energy (Mev)
0
5
10
2
3
4
5

Figure 22

Figure 23. Time spectrum at 8.0-Mev incident energy. The peaks near χ = 20 and 62 correspond to the 14.67- and 12.06-Mev B^9 states, respectively. The neutron group corresponding to the 14.0-Mev state appears as a slight distortion of the background continuum in the region χ = 40-50. The time scale was calibrated by the $Li^7(p,n)Be^7$ spectrum of Figure 25. See pp. 22, 26, 29, 38, 52-55.

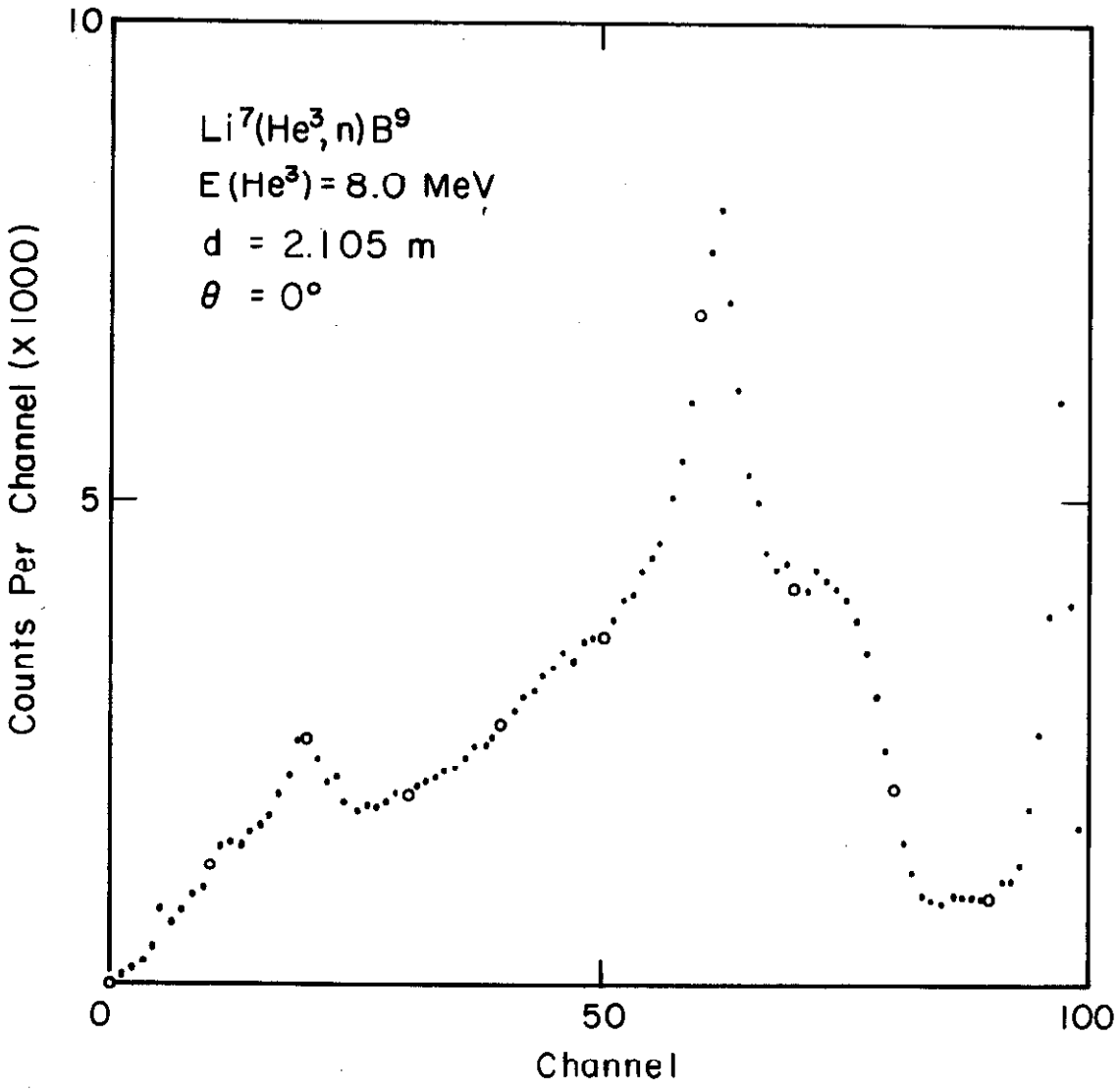
10
5
0
50
100
Channel
Counts Per Channel (X 1000)
Li7(He3, n)B9
E(He3) = 8.0 MeV
d = 2.105 m
θ = 0°

Figure 23

Figure 24. A portion of the spectrum of Figure 23 converted to the counts-vs.-energy presentation by the computer program described in Appendix A. The neutron groups corresponding to the B^9 levels at 14.67, 14.0, and 12.06 Mev may be seen near E_n = 1, 2, and 4 Mev, respectively. The best values for the excitation energies and widths of the 14.0- and 14.67-Mev levels were obtained from this spectrum. The dashed line represents the estimated level of the continuum. See pp. 22, 28-32, 36, 56.

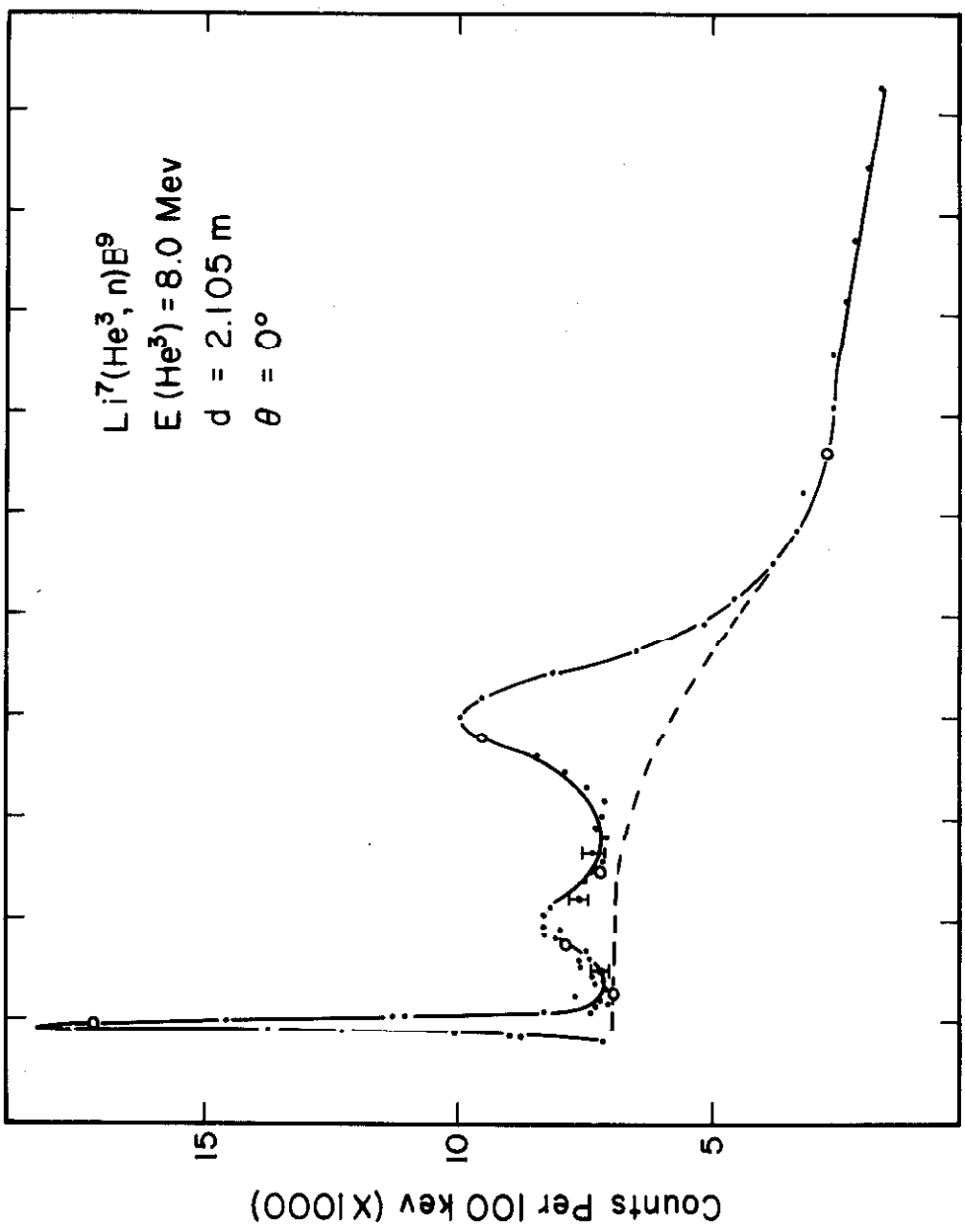
$Li^7(He^3, n)E^9$
E (He^3) = 8.0 Mev
d = 2.105 m
θ = 0°
Counts Per 100 kev (X1000)
Neutron Energy (Mev)
0
1
2
3
4
5
6
7
8
9
10
5
10
15

Figure 24

Figure 25. The $Li^7(p,n)Be^7$ spectrum which was used to calibrate the time scale for the spectrum of Figures 24-25. The peak near $\chi = 19$, corresponding to the Be^7 ground state, has energy $E_n = 1.0$ Mev. See pp. 26-29, 52, 55.

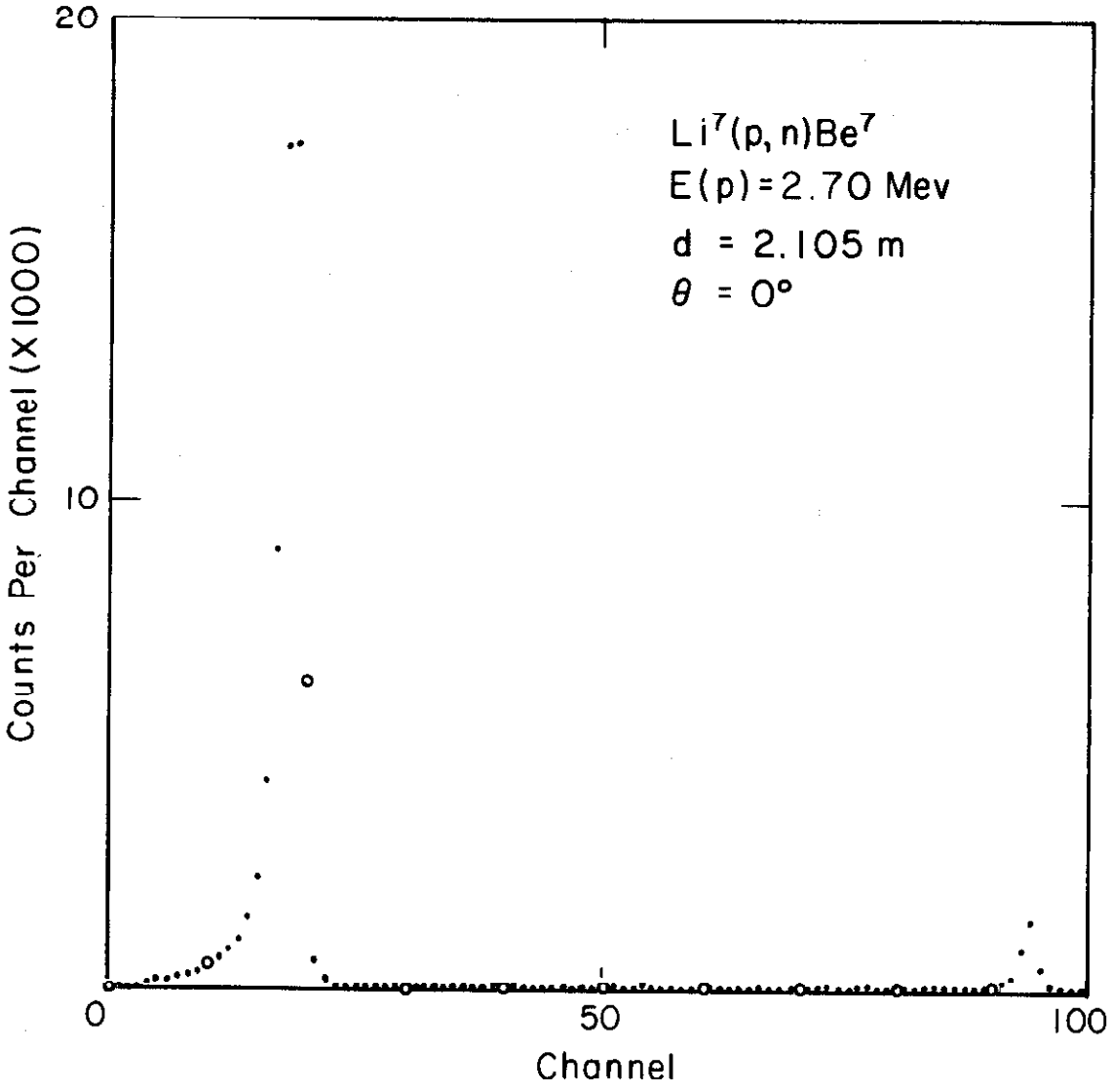
20
10
0
50
100
Counts Per Channel (X 1000)
Channel
Li⁷(p, n)Be⁷
E(p) = 2.70 Mev
d = 2.105 m
θ = 0°

Figure 25

Figure 26. The random time spectrum which was used to establish a time scale for the spectra of Figures 23-25, as explained in Appendix A, Section 4. The random time spectrum was obtained by placing a Cs^{137} gamma source in front of the detector. If the time scale were perfectly linear, the random time spectrum would be flat. The computer analysis described in Appendix A generates a correct time scale from the shape of the random time spectrum. See pp. 29, 53, 55.

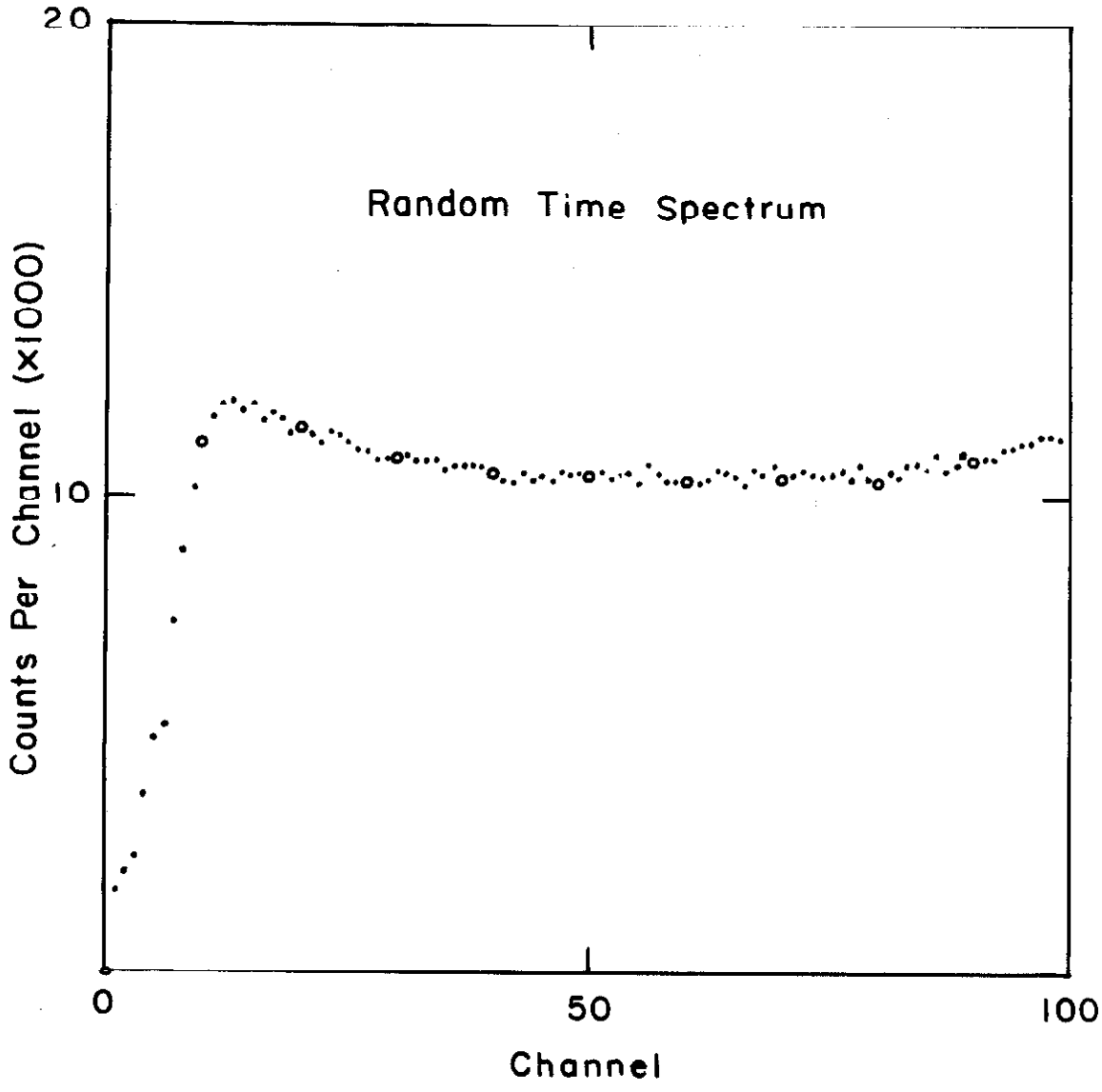
20
10
0
50
100
Random Time Spectrum
Counts Per Channel (X1000)
Channel

Figure 26

Figure 27. Angular distribution of neutrons corresponding to the 14.67-Mev B^9 level in the $Li^7(He^3, n)B^9$ reaction, at 8.7-Mev incident energy. See p. 27.

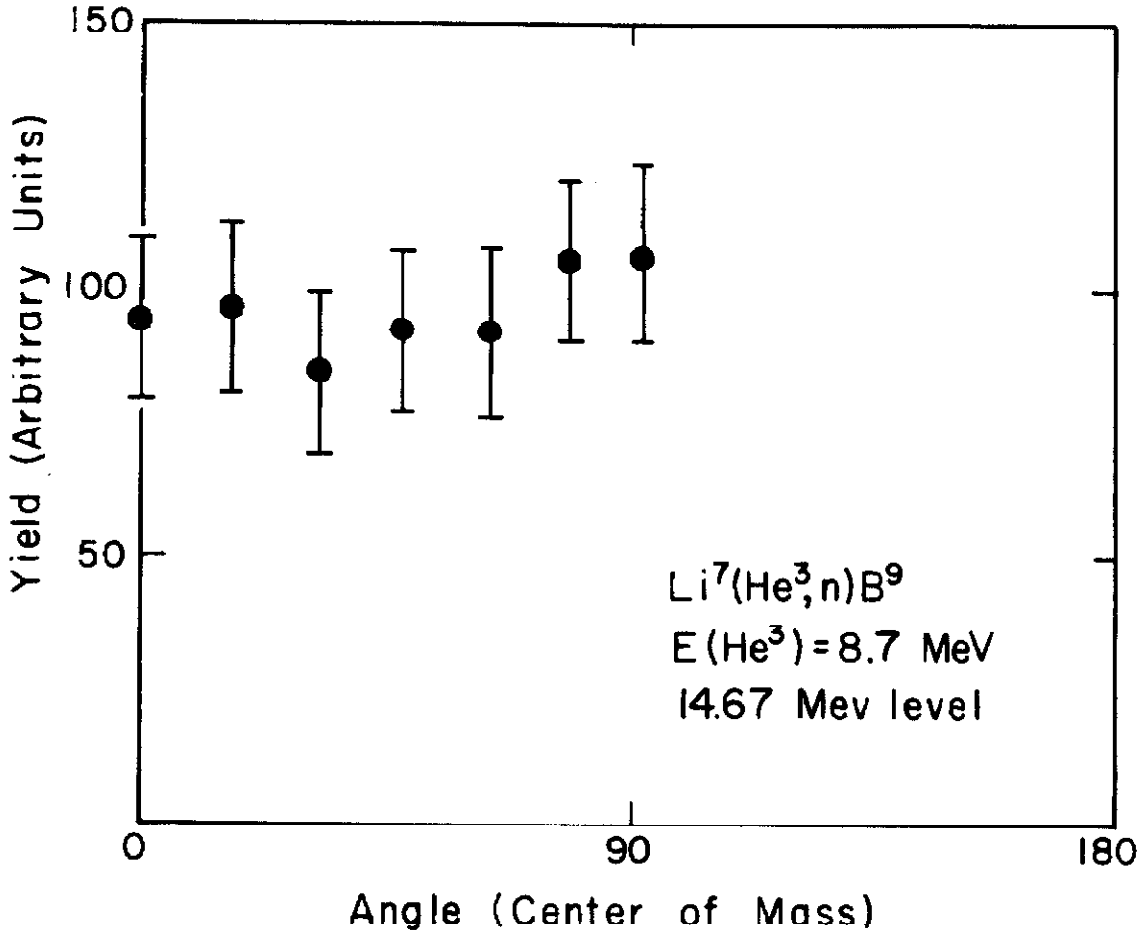
150
100
50
Yield (Arbitrary Units)
0
90
180
Angle (Center of Mass)
Li7(He3,n)B9
E(He3)=8.7 MeV
14.67 Mev level

Figure 27

Figure 28. Time spectrum at 8.7-Mev incident energy. This spectrum was one of nine used to determine the 0° differential cross section for the 14.67-Mev B^9 level. The neutron group corresponding to the 14.67-Mev B^9 level appears near $\chi = 36$. See p. 27.

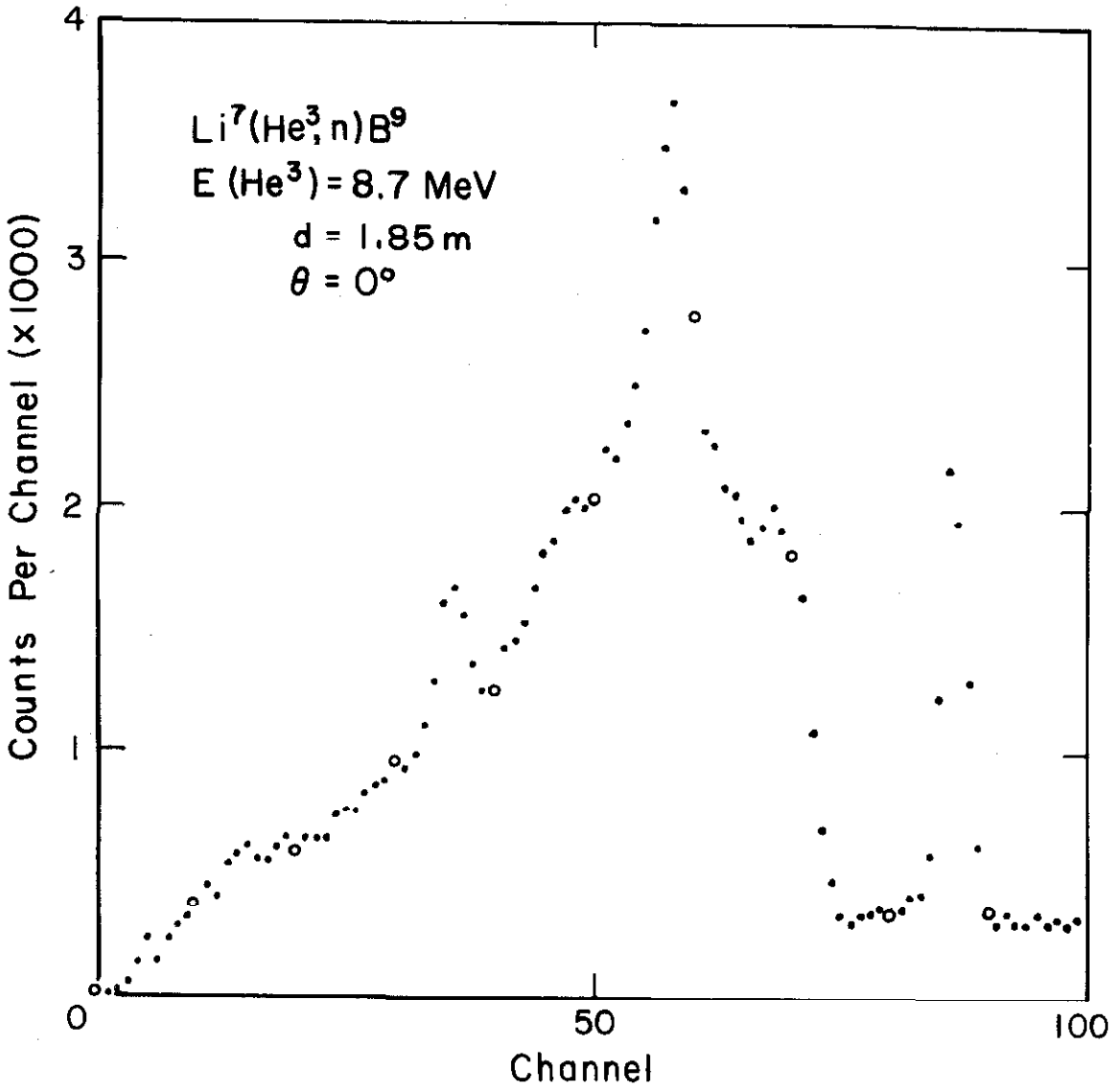
Li⁷(He³, n)B⁹
E (He³) = 8.7 MeV
d = 1.85 m
θ = 0°
Counts Per Channel (x1000)
Channel
0
1
2
3
4
50
100

Figure 28

Figure 29. Time spectrum at 6.25-Mev incident energy. The structure in the region χ = 20-40 corresponds to the 12.06-Mev B^9 state. This spectrum was calibrated by the $Li^7(p,n)\,Be^7$ spectrum of Figure 31. The small group near χ = 20 is a spurious gamma peak. See p. 32.

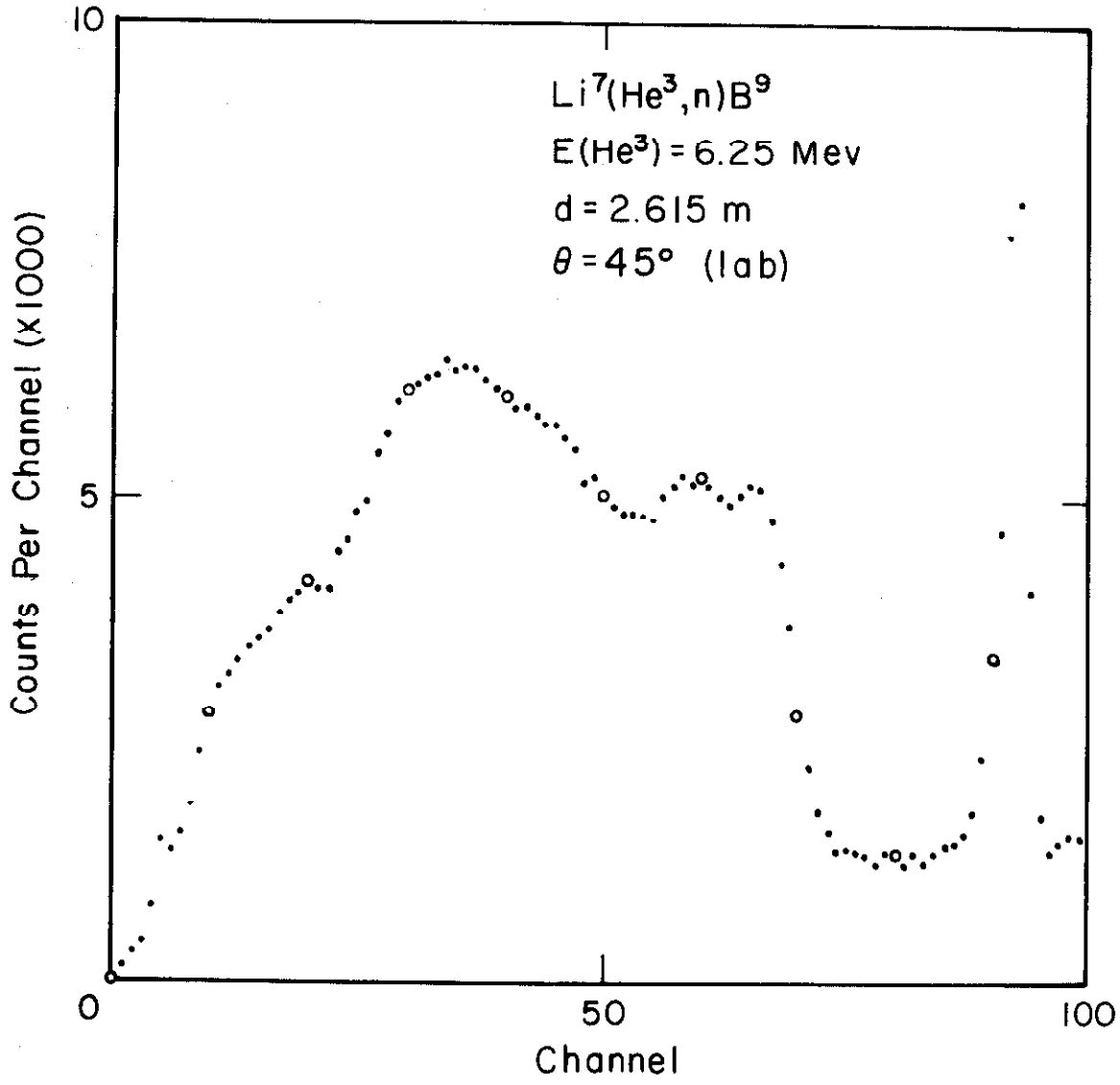
10
5
0
50
100
Counts Per Channel (x1000)
Channel
Li7(He3,n)B9
E(He3) = 6.25 Mev
d = 2.615 m
θ = 45° (lab)

Figure 29

Figure 30. A portion of the spectrum of Figure 29 converted to the counts-vs.-energy presentation. This spectrum provides the best value for the excitation energy of the 12.06-Mev B^9 level. The peak of the neutron group corresponding to the 12.06-Mev level occurs near $E_n = 2.1$ Mev. There is no evidence in this spectrum for a level at $E_x = 11.6$ Mev. See p. 32.

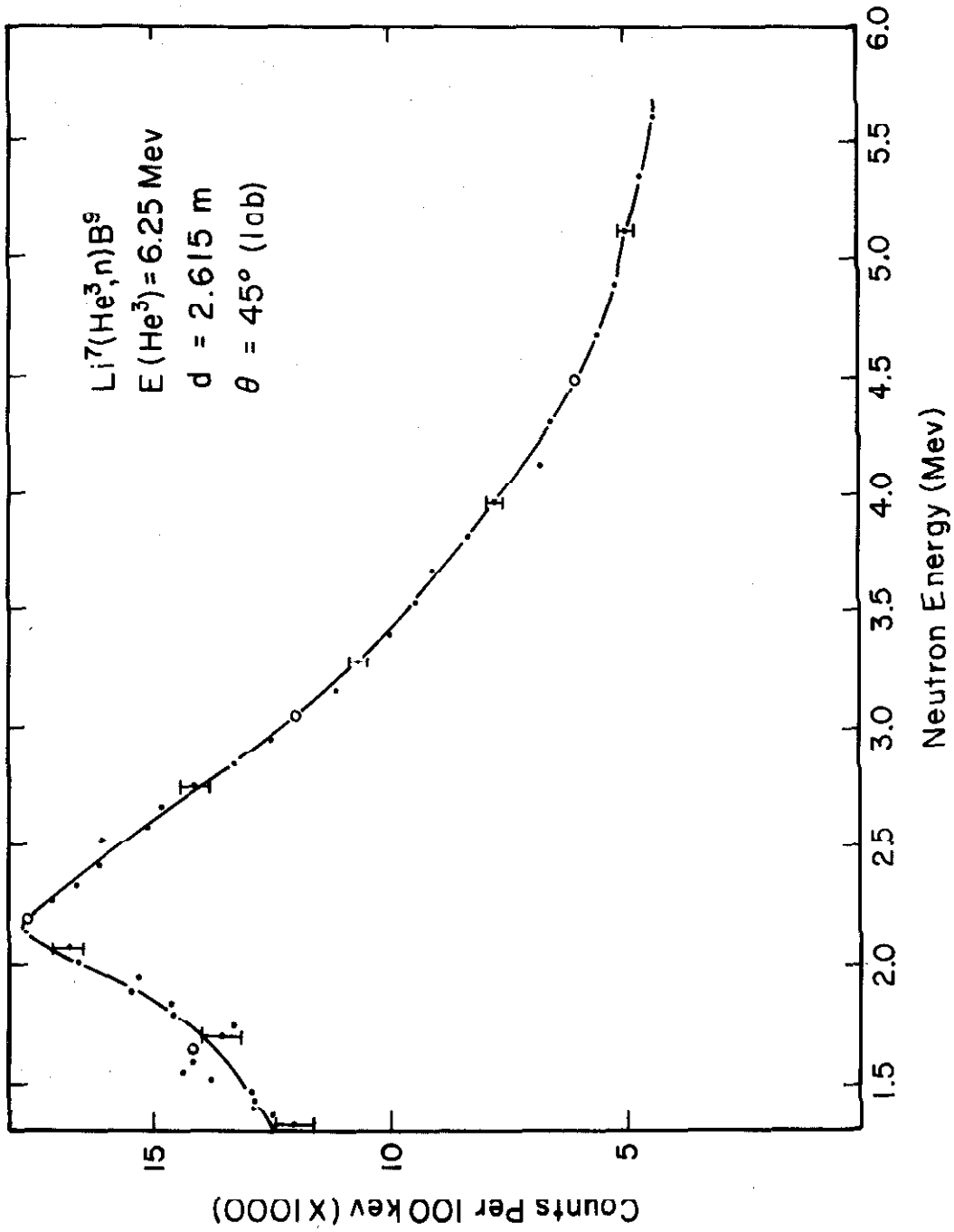
$Li^7(He^3,n)B^9$
E (He^3) = 6.25 Mev
d = 2.615 m
θ = 45° (lab)
Counts Per 100 kev (X 1000)
Neutron Energy (Mev)
15
10
5
1.5
2.0
2.5
3.0
3.5
4.0
4.5
5.0
5.5
6.0

Figure 30

Figure 31. Time spectrum of the $Li^7(p,n)Be^7$ reaction at 3.434-Mev incident energy. This spectrum was used to calibrate the time scale for the spectrum of Figures 29-30. The peak near $\chi = 19$ corresponds to the Be^7 ground state. The peak at $\chi = 5$, which falls in the unreliable portion of the spectrum below $\chi = 12$, probably corresponds to the Be^7 level at $E_x = 0.432$ Mev. See p. 32.

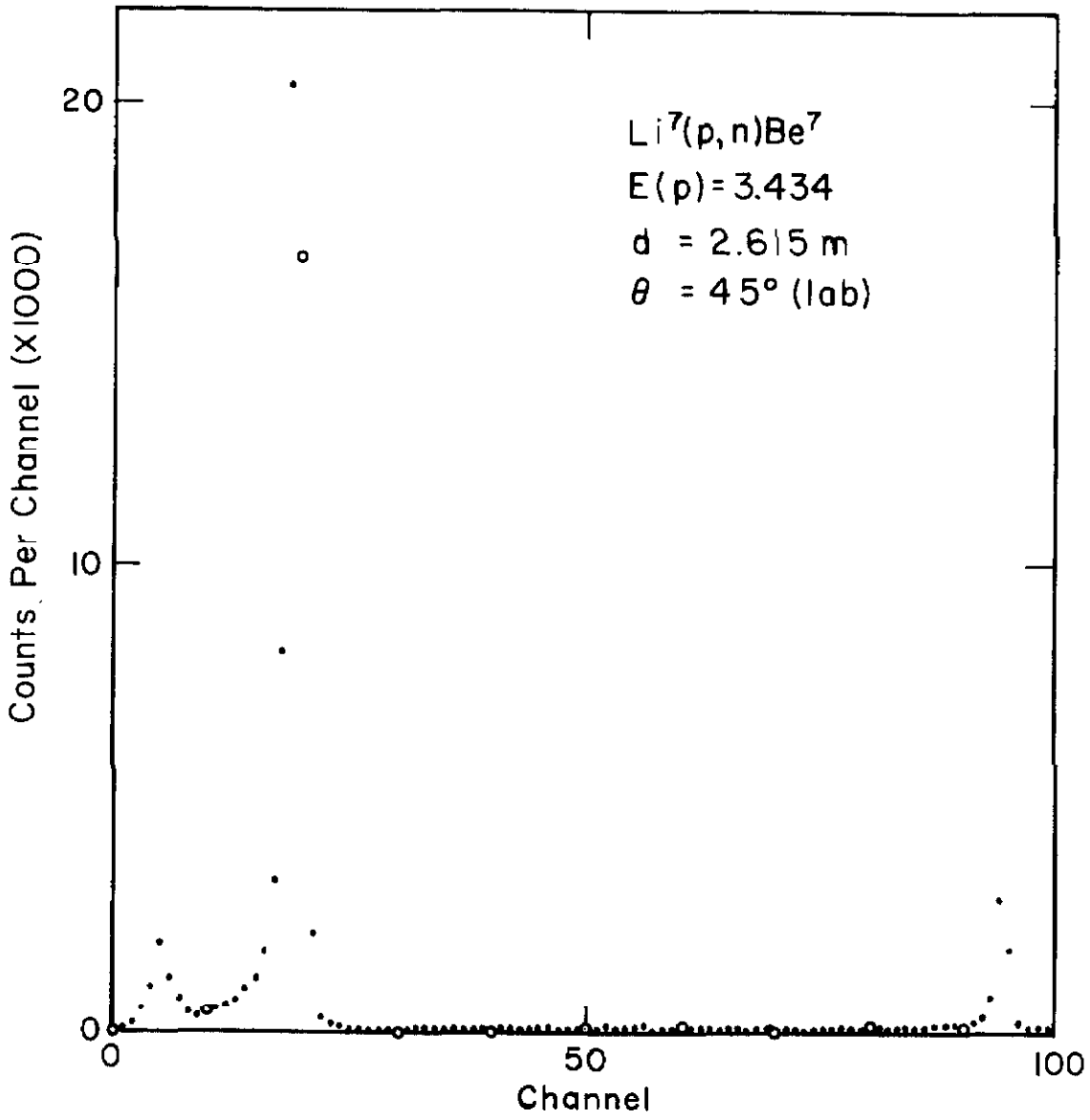
Li⁷(p,n)Be⁷
E(p) = 3.434
d = 2.615 m
θ = 45° (lab)
Counts Per Channel (X1000)
20
10
0
0
50
100
Channel

Figure 31